HAZ Liquation Cracking Mechanism of IN-738LC Superalloy Prepared by Laser Solid Forming

JIANJUN XU, XIN LIN, YUFAN ZHAO, PENGFEI GUO, XIAOLI WEN, QIUGE LI, HAIOU YANG, HONGBIAO DONG, LEI XUE, and WEIDONG HUANG

The heat-affected zone (HAZ) liquation cracking mechanism of nickel-based superalloys with high (Al + Ti) content during the laser solid forming (LSF) process was investigated *via* laser remelting of an as-deposited IN-738LC superalloy. Microstructural HAZ analysis revealed that cracks consistently propagated from the HAZ to the remelting zone along the grain boundary (GB). The formation of a liquid film during GB liquation was mainly owing to localized melting of the semicontinuous γ-γ' eutectic distributed along the GB. The solute segregation behavior of the IN-738LC alloy during LSF was analyzed using the Giovanola–Kurz model and Scheil models, revealing that a significant enrichment of γ-γ' eutectic-forming elements in the residual liquid at the final stage of solidification (solid fraction ~ 0.87) in the molten pool was the main cause of semicontinuous γ-γ' eutectic formation along the GB. Further, a B enrichment at the GB was identified in LSF-fabricated IN-738LC, which promoted cracking by lowering the GB liquation temperature and promoting wetting of the GB by the liquid film. Unlike the phenomenon observed in the welding of cast IN-738LC, the coherence between the γ' phases and the γ matrix in LSF-fabricated IN-738LC can suppress the occurrence of constitutional liquation of the γ' phase. To understand the interaction between the thermal stress and the liquid film in the LSF process, thermal stress as a cracking driving force was also estimated based on the measurement of the residual stress from the substrate to the remelting zone of the IN-738LC deposit by the Vickers micro-indentation method.

I. INTRODUCTION

THE precipitation-strengthened cast nickel-based superalloy IN-738LC is strengthened by precipitating the ordered Ni$_3$(Al,Ti)-γ' phase in the γ matrix. This alloy is widely used in the production of hot section components of both land-based and aeronautic gas turbine engine owing to its excellent high-temperature creep properties and remarkable resistance to hot corrosion.[1,2] In addition, laser solid forming (LSF) is a typical laser additive manufacturing technology that provides several advantages over the conventional cast process, such as the absence of dies, no size restrictions, fully dense structures, and high performance.[3,4] However, LSF is a layer-by-layer deposition process, and thus the heat accumulation and the reheating effect of subsequent depositions will cause the deposited layer to undergo a certain high-temperature heat treatment with the maximum treatment temperature close to the melting point. The previously deposited layer, as a heat-affected zone (HAZ), is prone to cracking during the subsequent deposition when the deposited materials present a high cracking susceptibility. Therefore, clarifying the cracking mechanism and avoiding cracking become key factors to ensure the high performance of LSF-fabricated parts.

Chen *et al.*[5] have achieved an LSFed IN-738LC thin-walled component with a reasonably good thermal stability after exposure to high temperature (845 °C) for 3 to 6 days. Further, Rickenbacher *et al.*[6] have produced an IN-738LC part with mechanical properties

JIANJUN XU, XIN LIN, PENGFEI GUO, XIAOLI WEN, QIUGE LI, HAIOU YANG, and WEIDONG HUANG are with the State Key Laboratory of Solidification Processing, Northwestern Polytechnical University, 127 Youyixilu, Xi'an, Shaanxi 710072, P.R. China and also with the Key Laboratory of Metal High Performance Additive Manufacturing and Innovative Design, MIIT China, Northwestern Polytechnical University, 127 Youyixilu, Xi'an, Shaanxi 710072, P.R. China. Contact e-mail: xlin@nwpu.edu.cn, yanghaiou@nwpu.edu.cn YUFAN ZHAO is with the Department of Materials Processing, Graduate School of Engineering, Tohoku University, 6-6-11 Aoba, Aramaki, Aoba-ku, Sendai 980-8579, Japan. HONGBIAO DONG is with the Department of Engineering, University of Leicester, Leicester LE1 7RH, UK. Contact e-mail: hd38@leicester.ac.uk LEI XUE is witn the Xi'an Bright Laser Technologies LTD, Xiyuan, Northwestern Polytechnical University, Western Part of South Second Ring Road, Xi'an 710072, Shaanxi, P.R. China.

Manuscript submitted March 12, 2018.
Article published online July 17, 2018.

superior to cast IN-738LC by selective laser melting (SLM), though cracking, which was found to be unavoidable in this part, limits further improvement of the part performance. The same problem also exists in the LSF-fabricated Rene 88DT alloy,[7] which is also a γ'-precipitation-strengthened nickel-based superalloy, wherein the cracking can be attributed to the high content of Al and Ti in these γ'-precipitation-strengthened superalloys (Al + Ti > 6 wt pct, generally). It should be noted that the crack behaviors in the laser additive manufacturing process are similar to that in the fusion welding process. Many previous works have attempted to explain the cracking mechanisms in the fusion welding of high-(Al + Ti)-content Ni-based superalloys and have confirmed that the cracks are owing to grain boundary (GB) liquation cracking in the HAZ. Further, the mechanisms governing GB liquation have been deemed as localized melting (also called direct liquation) of the γ-γ' eutectic or as constitutional liquation of γ' particles and carbides.[8–12]

It is well known, however, that the susceptibility of a secondary phase to constitutional liquation is primarily related to its solid-state dissolution behavior, as shown in Figure 1. Constitutional liquation was first proposed by Pepe and Savage,[8,13] and usually occurs below an alloy's equilibrium solidus temperature and can be described as follows: During the rapid heating process, the solute concentration in the matrix at the precipitate/matrix interface will increase with the solid-state dissolution of the precipitate (light-red ringed zone in Figure 1). When that solute concentration exceeds the alloy composition at a temperature equal to or above the equilibrium reaction temperature of the precipitate–matrix eutectic, a metastable solute-rich liquid film will be formed at the precipitate/matrix interface, thus inducing the constitutional liquation (*i.e.*, a subsolidus liquation) to occur. Subsequently, the adjacent liquation zones will connect to form a liquid film and will eventually crack under tensile stress (shown in Figure 1). According to a previous work, the solid-state dissolution process of a non-coherent precipitate is typically diffusion-controlled, and constitutional liquation can occur easily. Conversely, the solid-state dissolution of a coherent precipitate is usually interface-controlled, and the constitutional liquation will not occur.[14] Interestingly, once the particles (such as the γ' phase in nickel-based superalloys) exceed a critical dimension, a coherency loss will occur.[15–18] Considering that the sizes of the γ-γ' eutectic, γ' particles, and carbides in the LSF-fabricated nickel-based superalloys are much smaller than those in cast superalloys,[5,19] however, it remains a controversy whether or not constitutional liquation occurs in LSF-fabricated nickel-based superalloy. Zhao *et al.*[20] have found that the cracks in LSF-fabricated Rene 88DT alloy (Al + Ti of ~ 5.5) are primarily liquated cracks resulting from the localized melting of the γ-γ' eutectic (shown in Figure 1) in the previously deposited layer owing to the reheating
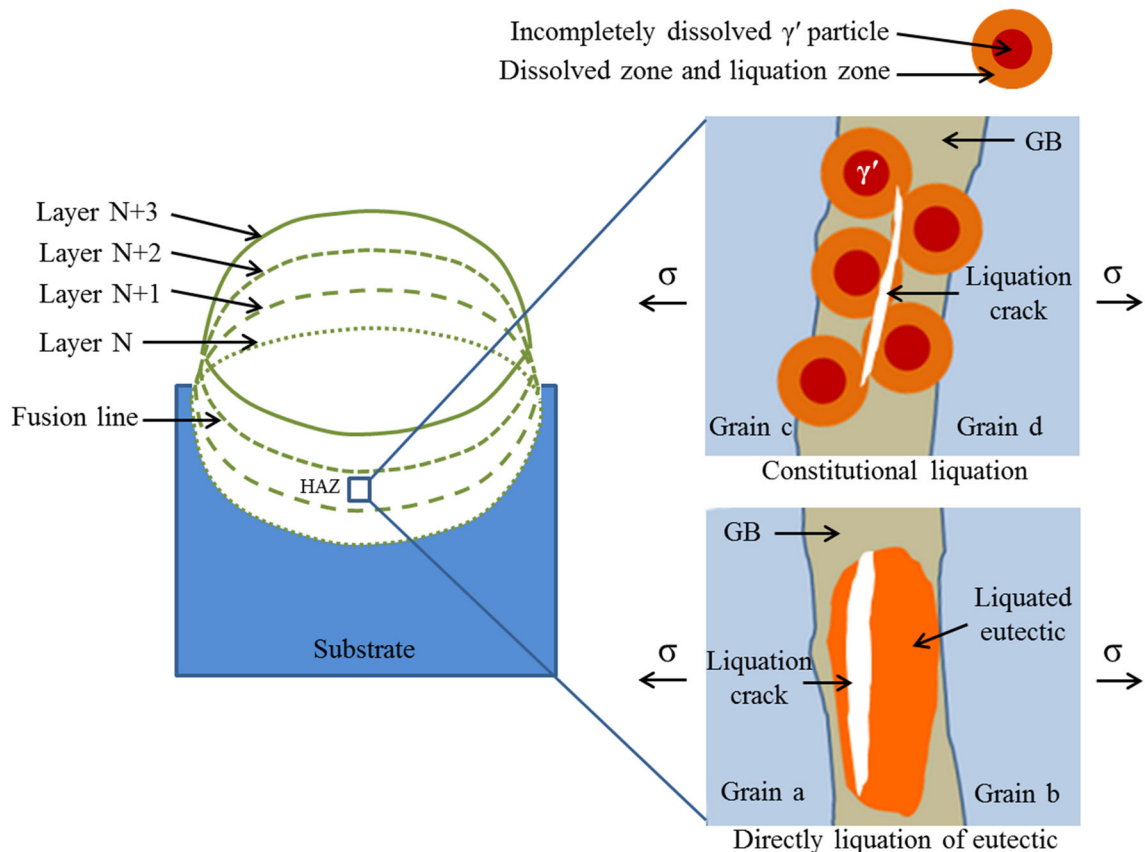

Fig. 1—Schematic diagram of constitutional liquation and direct liquation (localized melting) of the low-melting-point eutectic.

from the subsequent laser deposition, and no constitutional liquation is found. In contrast to Zhao et al.'s findings, Yang et al.[21] still attribute the GB liquation to the constitutional liquation of γ' particles in LSF-fabricated Rene 104 superalloy (Al + Ti of ~ 7.1) and the liquid film separates into cracks under tensile stress, as shown in Figure 1.

Importantly, once the cracks are formed, their initial morphology will be affected by the subsequent laser deposition during LSF, in which the thermal history can be very complex, including melting, solidification, remelting, partial-remelting, cyclic annealing, etc. (Figure 1). Thus it is challenging to find direct evidence of GB liquation, which causes the controversy regarding the liquation cracking mechanism during LSF. In the present work, the laser remelting of an IN-738LC alloy deposit fabricated by LSF was carried out. Crack analysis combined with microstructural observation and microsegregation analysis was conducted on the laser remelting of the LSF-fabricated IN-738LC alloy, which will provide theoretical support for future extensive applications of LSF technology in superalloys with a high (Al + Ti) content.

II. EXPERIMENTAL PROCEDURES

The substrate used for laser remelting was an LSF-fabricated IN-738LC alloy deposit, whose chemical composition is listed in Table I. The substrate with dimensions of $15 \times 5 \times 10$ mm^3 was fabricated by an LSF system comprising a 1kW YAG laser, a four-axis numerical control working table, and a powder feeding system with a coaxial nozzle. The surface of the substrate was polished and subsequently cleaned thoroughly with acetone before laser remelting.

The upper portion of the LSF-fabricated IN-738LC alloy was cut into two parts by a wire electro-discharge machining device, as shown in Figure 2. One was used for laser remelting, which was carried out using the LSF system and whose processing parameters are listed in Table II. Another was rapidly heated by a Gleeble 3500 thermomechanical simulation system to study the GB liquation. Because the γ-γ' eutectic transformation in the IN-738LC alloy occurs over a range of temperatures that could be below 1120 °C,[22] the $15 \times 5 \times 10$ mm^3 deposit was rapidly heated to 1160 °C at a rate of 20 °C/s, was then held for 1 second at 1160 °C, and was subsequently quenched with water (Figure 2).

A transverse section was cut from the remelted specimen via a wire electro-discharge machining, whereupon the cut specimens were chemically etched (5 g FeCl$_3$, 20 ml HCl + 100 ml C$_2$H$_5$OH) for optical metallography. The cut specimens were further etched electrolytically in a solution of 12 ml H$_3$PO$_4$ + 48 ml H$_2$SO$_4$ + 40 ml HNO$_3$ to reveal the morphology of the

γ-γ' eutectic, γ' particles, and carbides. The microstructure was subsequently observed with an OLYMPUS-GX71 optical microscope (OM), a TESCAN MIRA3 XMU field emission scanning electron microscope (FE-SEM), and a TECNai F30 G2 transmission electron microscope (TEM). The chemical composition at various specimen positions was analyzed by a SHIMADZU-1720 electron probe microanalysis technique (EPMA). The Thermo-Calc Software was employed for the calculation of the solidification sequence of the IN-738LC alloy.

On considering the close relationship between the dynamic thermal stress and the final residual stress, the residual stress of the deposits was investigated using the Vickers micro-indentation method,[23,24] where the microhardness was tested on a LECO automatic hardness testing system. The stress–strain curve of the LSF-fabricated IN-738LC alloy was obtained by testing an as-deposited sample with the tensile axis parallel to the laser scanning direction. The room-temperature tensile test was performed on an INSTRON11-3382 tensile testing machine with a displacement rate of 2 mm/min. Two assumptions were made here, where the first is that the residual stress is in an equal-biaxial state and the second is that the uniaxial stress–strain curve obeys the power-law function $\sigma = K\varepsilon_p^n$, where K and n are material constants that can be obtained from the uniaxial stress–strain curve. Anisotropy of the microstructure and tensile properties does exist in the LSF-fabricated parts. According to literature,[6] however, the difference in the yield strength and ultimate tensile strength of the LSF-fabricated IN-738LC in the directions parallel and perpendicular to the deposition direction can be 15 to 18 pct and just about 1 pct, respectively, which are all less than 20 pct. Thus, it is reasonable to assume that the stress states in the two directions are approximately at the same level. Further, the errors of the residual stress estimated based on the microhardness, which is usually proportional to the strength, should be less than 20 pct. Therefore, this method remains one of the most common for measuring residual stress of the LSF-fabricated alloys.[25,26] The residual stress and the residual strain have been reported to follow the following relations:[27]

$$H = C\sigma(\varepsilon_{\text{repr}} + \varepsilon_{\text{res}}), \qquad [1]$$

$$c^2 = c_0^2 - 0.32 \ln\left[1 + \frac{\sigma_{\text{res}}}{\sigma(\varepsilon_{\text{res}})}\right], \qquad [2]$$

where, H is the microhardness of the deposits, C a constant that depends on the geometry of the sharp indenter, $\varepsilon_{\text{repr}}$ the representative value of the effective plastic strain, ε_{res} the residual von Mises effective plastic strain in an equi-biaxial situation, $\sigma(\varepsilon_{\text{repr}} + \varepsilon_{\text{res}})$ the flow stress at an effective plastic strain ($\varepsilon_{\text{repr}} + \varepsilon_{\text{res}}$),

Table I. Chemical Composition of the IN-738LC Powders (Weight Percent)

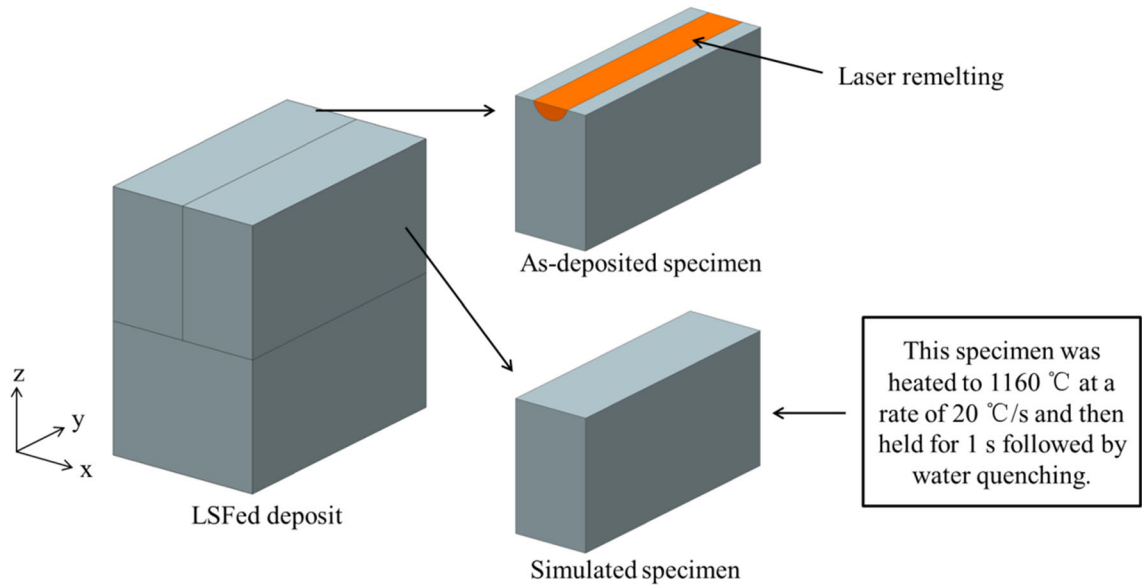| C	Cr	Al	Ti	Mo	W	Co	Nb	Ta	Si	Fe	B	Ni
0.11	15.79	3.4	3.4	1.77	2.54	8.25	0.8	1.74	0.049	0.078	0.008	bal.

Fig. 2—Schematic diagram of the specimen sections used for laser remelting and that used for rapid heating *via* the thermomechanical simulation system.

Table II.   Laser Remelting Processing Parameters

Laser Power (kW)	1
Scanning Speed (mm/min)	400
Spot Diameter (mm)	2

and c^2 the area ratio between the real projected contact area A and the nominal projected contact area A_{nom} of the diamond indentation such that $c^2 = A/A_{nom}$. The nominal projected contact area of diamond indentation can be defined as $A_{nom} = [(L_1 + L_2)/2]^2/2$, where L_1 and L_2 are the length of the diagonal line of the sharp indenter. According to the work by Liu,[25] $C = 3$, $\varepsilon_{repr} = 0.08$ and $c_o^2 \approx 1$. Thus, substituting these parameters into Eqs. (1) and (2), the residual strain (ε_{res}) and the residual stress (σ_{res}) were obtained as follows:

$$\varepsilon_{res} = \left(\frac{H}{3K}\right)^{1/n} - 0.08, \qquad [3]$$

$$\sigma_{res} = K|\varepsilon_{res}|^n \left[\exp\left(\frac{c^2 - 1}{0.32}\right) - 1\right]. \qquad [4]$$

Note that the presented analysis cannot distinguish between the tensile and compressive stresses but this does not affect the analysis of the cracking driving force because of the following reason: On the one hand, the residual stress state (tensile/compressive) in the remelted IN-738LC deposit should be similar to that in a welded specimen. In general, the liquid in the welding pool and the liquid film formed in the HAZ will be stretched by the surrounding matrix during solidification following the welding. Thus there typically exists both residual tensile stress in the fusion zone and the HAZ as well as

residual compressive stress in the substrate away from the HAZ, which has been shown in the works of Chamanfar and Bonakdar.[28,29] On the other hand, the true driving force of HAZ cracking is the thermal stress generated during the rapid heating and cooling. In that situation, the HAZ temperature is still high and the liquid film formed in the HAZ is typically stretched by a tensile stress to form the cracks. Thus, an equivalent stress was estimated herein to reflect the thermal stress formed during the LSF process, which can aid in understanding the HAZ cracking driving force.

III.   RESULTS

A. *Microstructure of the As-deposited IN-738LC*

It is well known that the formation temperature of the low-melting-point phase of will affect whether it is easily liquated. Figure 3 shows the solidification sequence of the IN-738LC alloy as calculated by Thermo-Calc software under the equilibrium and Scheil models using the TTNi database.[30] It was found that the primary γ phase was formed at 1343.7 °C, after which the carbide formed at 1330.6 °C. Finally, the solidification terminated at 1288.7 °C after the formation of a small amount of boride at 1290.5 °C. After the solidification, the γ' phase was precipitated from the γ matrix at 1135.7 °C (Figure 3(a)). However, the Scheil model, which considers the solute redistribution during solidification, predicted that the formation of the σ phase (a common phase in superalloys) occurred at 1150.9 °C and the γ-γ' eutectic reaction occured at 1118.8 °C, which is after the formation of carbide at 1330.1 °C and boride at 1214.7 °C (Figure 3(b)).

The case of rapid cooling, however, will cause the microsegregation behavior of the elements to vary from the thermodynamic equilibrium prediction during LSF
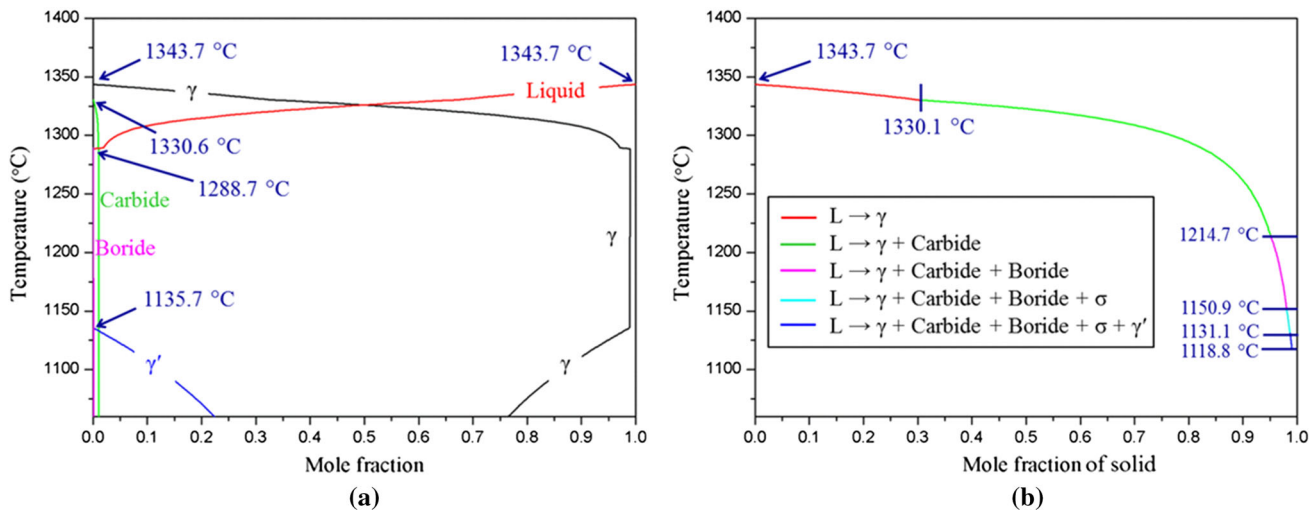
Fig. 3—Equilibrium phases and their weight fractions in the IN-738LC alloy at each temperature as predicted by Thermo-Calc (*a*) and the solidification sequence as calculated by the Scheil model (*b*).
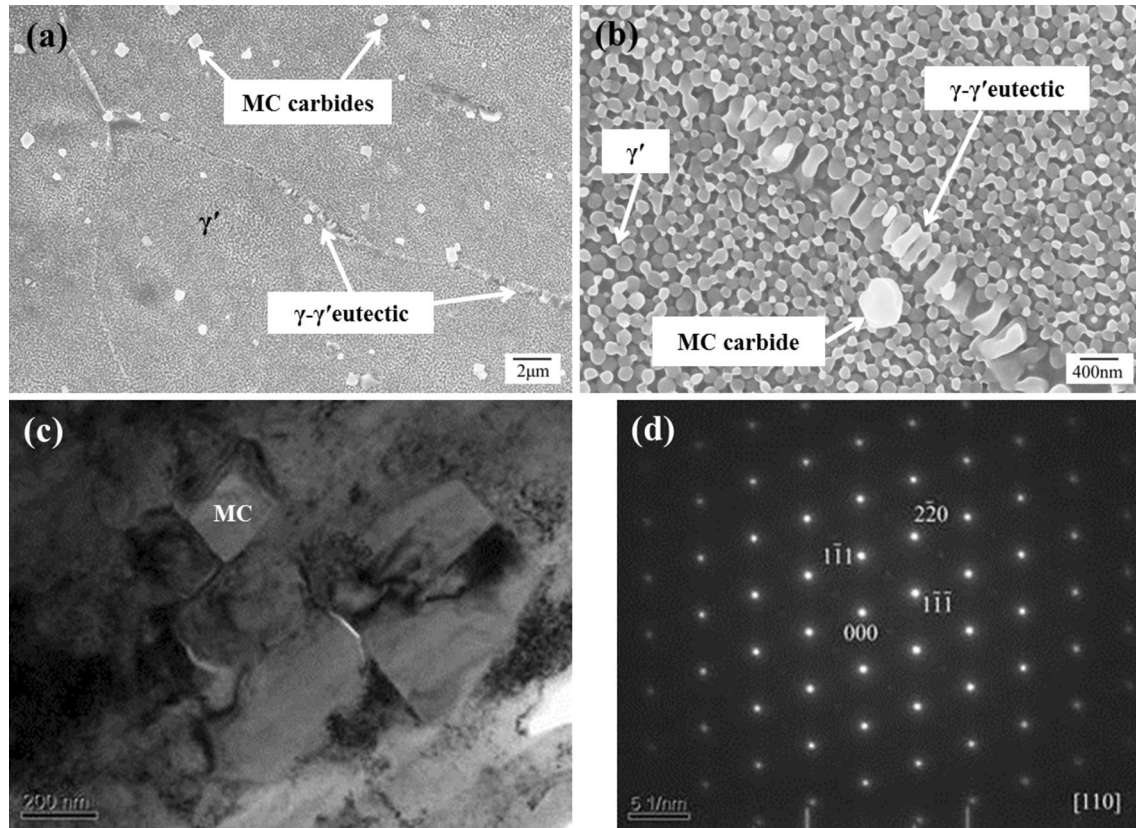

Fig. 4—Low- (*a*), high- (*b*) magnification SEM micrographs showing the microstructure of as-deposited IN-738LC alloy and TEM micrograph of blocky MC carbide (*c*) with the SADP from the [110] zone axis (*d*).

(*i.e.*, a near-rapid solidification process).[31] The typical microstructure of the as-deposited IN-738LC alloy is shown in Figure 4. Note that the GB mainly consists of semicontinuous γ-γ' eutectic and small amount of carbides (Figure 4(a)), while no σ phase was observed. The higher-magnification image of the microstructure shows the regular lamellar γ-γ' eutectic at the GB

(Figure 4(b)). The composition at the GB region, at which the lamellar constituent is located, was measured by EPMA and is listed in Table III. The composition of the liquid as predicted by the Scheil model at the γ-γ' eutectic-forming temperature (1131.1 °C) is listed in Table III. The actual measurement area may exceed the range of the lamellar constituents owing to its very small

size, and thus the actual microsegregation during LSF may deviate from the theoretical prediction. Thus a deviation exists between the measured and theoretically predicted values. However, it can still be seen that the contents of the γ-γ′ eutectic-forming elements Ti, Al, Nb, and Ta, and especially Ti, are clearly higher than the nominal composition in the IN-738LC alloy, which is consistent with the predicted values. Thus, the lamellar constituent should be γ-γ′ eutectic. Note that discontinuous coarsening of some GB constituents may have occurred during LSF owing to the fact that the heat accumulation in the deposited layers will increase significantly with continued deposition, which is equivalent to a heat treatment. Thus, some of the GB constituents do not appear to have the typical eutectic morphology. The carbide exhibits an irregular blocky shape and the γ′ phases exhibit a spherical shape with a diameter of about 100 nm. Figure 4(c) shows a TEM micrograph of the blocky carbide with the selected area diffraction pattern (SADP) from the [110] zone axis (Figure 4(d)), which confirms the carbide as an MC-type.

B. Microstructure of the Laser Remelting of the As-deposited Specimen

Figure 5 is an optical micrograph showing the cracks in the laser remelting of the as-deposited IN-738LC alloy. As shown in Figure 5(a) the molten pool mainly consists of columnar grains growing epitaxially from the substrate deposit, while the cracks generally occur in the HAZ. The higher-magnification optical micrograph (Figure 5(b)) shows that the cracks only form along the GBs, and Figure 5(c) shows the dendrites with secondary arms and the continuous GBs.

Figure 6 shows the microstructure of the laser remelting of the HAZ close to the remelting zone (RZ). Combining Figure 4(a) with Figures 6(a) and (b), it is revealed that only the γ matrix and irregular blocky carbides (called stable carbides in this work) can be found in the HAZ near the RZ. As shown in Figures 6(c) and (d), the crack, located at the GB according to Figure 5, exhibits the irregular and zigzag morphology typical of liquation cracking.

Figure 7 shows the microstructure of GBs away from the RZ in the HAZ. As shown in Figure 7(a), there is an apparent liquation of the γ-γ′ eutectic, and a continuous liquid film is thus formed along the GB. The γ′ phases dissolve into the γ matrix incompletely while the MC carbides maintain their shape and size almost unchanged compared with that in the substrate deposit shown in Figure 1. A crack is observed to form preferentially along the intergranular liquid film which results from the liquation of the γ-γ′ eutectic located at the edge of the crack, as shown in Figure 7(b).

The substrate deposit was reheated to 1160 °C for 1 second and then was water-quenched in the thermomechanical simulation system, with the goal of simulating the possible microstructure evolution present in the HAZ during laser remelting/reheating. As shown in Figure 8, the liquated γ-γ′ eutectic and liquid film formed along the GB can also be found in the reheated deposit. Micropores exist in the liquid film (Figure 8(a)), which indicates that cracks were initially formed by liquid film separation. The liquid film was stretched until ultimately cracking was induced (Figure 8(b)). It is generally known that the γ′ phase in the interdendritic region is larger than that in the dendrite in the γ′-strengthened Ni-based superalloy, while the γ′ phase of the IN-738LC alloy was observed to begin to dissolve at about 1000 °C by differential scanning calorimetry.[32] Because the reheating temperature was well above the predicted equilibrium γ′ solvus and should therefore be even farther above the solvus temperature of the dendrite core γ′, the γ′ phases in the dendrite core should be completely dissolved while those in the interdendritic region should undergo incomplete dissolution during the reheating (Figure 8).

To understand the relationship between the cracks and the local compositional enrichment in the GBs, the elemental distribution around the crack was determined by EPMA and is shown in Figure 9. It can be noted that C, Ti, Nb, Ta, and Mo are enriched at the interdendritic region and GB (crack region), while Co is clearly enriched at the dendrite core. Meanwhile, the crack core exhibits a lack of Al, which is the main forming element of the γ-γ′ eutectic, owing to the relatively weak segregation capacity of Al in the nickel-based superalloy.[31,33] Interestingly, the results of the EPMA show a slight enrichment of B at the GB, as shown in Figure 9. According to the calculated partition coefficient ($k′ = C_{\mathrm{core}}/C_0$) given in Table III, while the cooling rates in the laser processes are indeed very high, they typically are not high enough to induce solute trapping and therefore significantly reduced segregation behavior. But the high cooling rate will cause the borides to be unable to fully precipitate and grow in size. Therefore, the size of the boride would be too small to be easily observed under the SEM owing to the very low content of B (only about 0.008 wt pct).

IV. DISCUSSION

A. Formation Mechanism of Continuous/Semicontinuous γ-γ′ Eutectic Along GB

As stated earlier, one of the most important factors causing HAZ cracking is the formation of a continuous liquid film distributed along the GB, which is closely related to the microstructure in the deposit.[34] It is therefore necessary to understand the microsegregation and formation of solidification constituents in the LSF-fabricated IN-738LC alloy before discussing the liquation phenomenon.

Figure 5(c) clearly shows a dendritic microstructure and the average secondary dendrite arm spacing was measured about at 5.5 μm. Its cooling rate was estimated to be about 127 °C/s according to the empirical relationship between the cooling rate and secondary dendrite arm spacing for IN-738LC:[35]

$$\lambda_2 = 196.8 V_{\mathrm{c}}^{-0.4}, \quad [5]$$

where λ_2 is the secondary dendrite arm spacing and V_{c} is the cooling rate. This cooling rate is considerably

Table III. EPMA Quantitative Results (Weight Percent) at the GB and Dendrite Core Region, Scheil Model-Predicted γ-γ′ Eutectic Composition, and the Calculated Partition Coefficient ($k' = C_{core}/C_0$) of the Main Elements in the IN-738LC Alloy

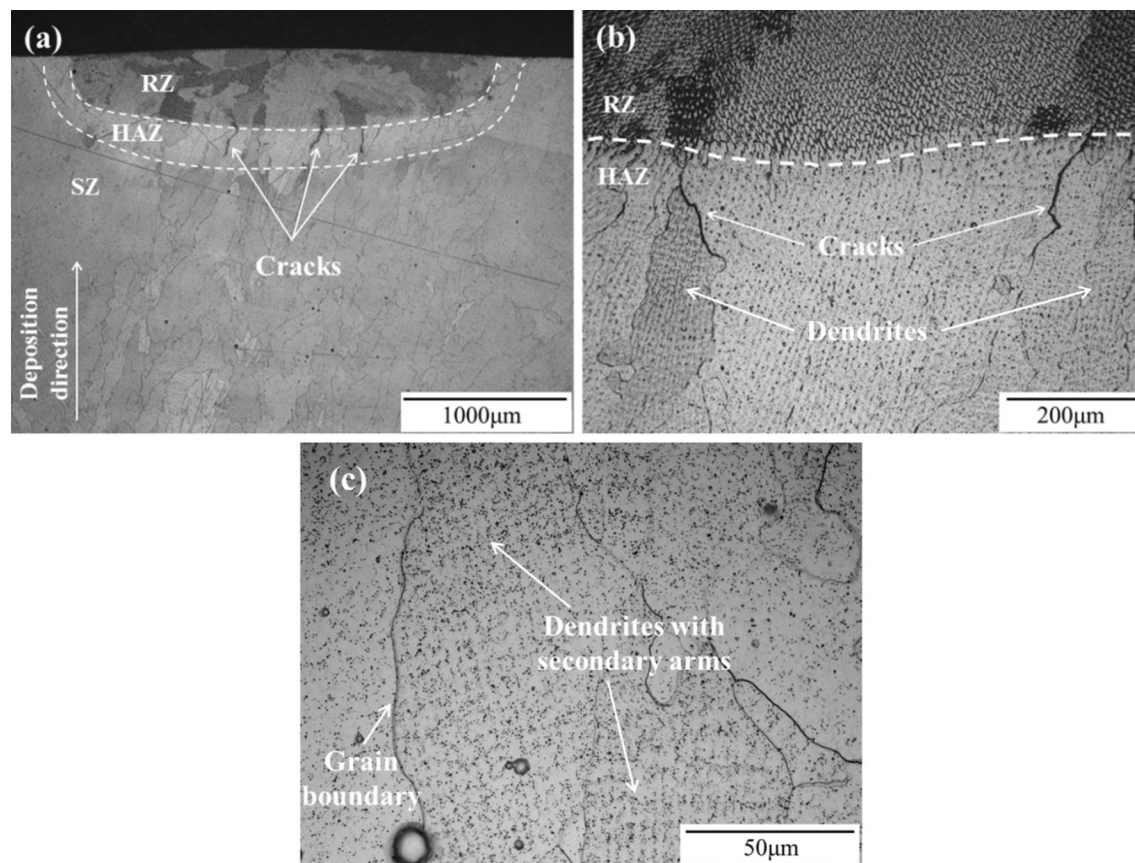|	Cr	Al	Ti	Mo	Co	Nb	Ta	C	Ni
GB	16.99	3.36	5.46	1.84	7.68	1.81	3.17	0.21	—
Predicted γ-γ′ Eutectic	18.41	2.07	7.41	4.53	4.32	7.94	11.50	0.007	
Dendrite Core	15.54	3.42	2.16	1.35	8.81	0.44	1.01	0.04	—
k'	0.984	1.006	0.635	0.763	1.068	0.55	0.58	0.364	—

Fig. 5—Low- (a) and high- (b and c) magnification optical micrographs of the transverse section of the laser remelting in the as-deposited IN-738LC specimen showing its microstructure and the HAZ cracking.

more rapid than that in the conventional casting process. Accordingly, the relationship between the solid fraction (f_s) and the solute concentration in the solid (C_s^*) in the LSF-fabricated specimen can be described by the model proposed by Giovanola and Kurz (GK),[36] which takes into account non-equilibrium solute redistribution and dendrite tip undercooling:

$$f_s = a_1 C_s^{*2} + a_2 C_s^* + a_3 \ (0 \leq f_s \leq f_x),$$ [6]

$$f_s = 1 + (f_x - 1)(C_s^*/C_x)^{\frac{1}{k-1}} \ (f_x \leq f_s \leq 1),$$ [7]

where k is the non-equilibrium partition coefficient; f_x a critical value of the solid fraction; C_x the corresponding solute concentration in the solid; and where a_1, a_2, a_3, f_x, and C_x are unknown coefficients. Furthermore, at the dendrite tips ($f_s = 0$), the solute

content in the solid (C_{st}^x) can be determined by the Kurz–Giovanola–Trivedi model:[37]

$$C_{st}^* = C_0 k A,$$ [8]

$$k = \frac{k_0 + (a_0 V/D)}{1 + (a_0 V/D)},$$ [9]

where C_0 is the initial alloy concentration, $A = 1/(1 - (1 - k)I_v(P))$, $I_v(P)$, the Ivantsov function of the solute Peclet number,[38] k_o the equilibrium partition coefficient, V the growth velocity of dendrites approximated by the scanning speed, a_0 a length scale related to the interatomic distance, and D the solute diffusion coefficient in the solid–liquid interface. Setting $f_s = 0$ for $C_s^* = C_{st}^*$, the five unknown coefficients above will have the following relationships:[36]
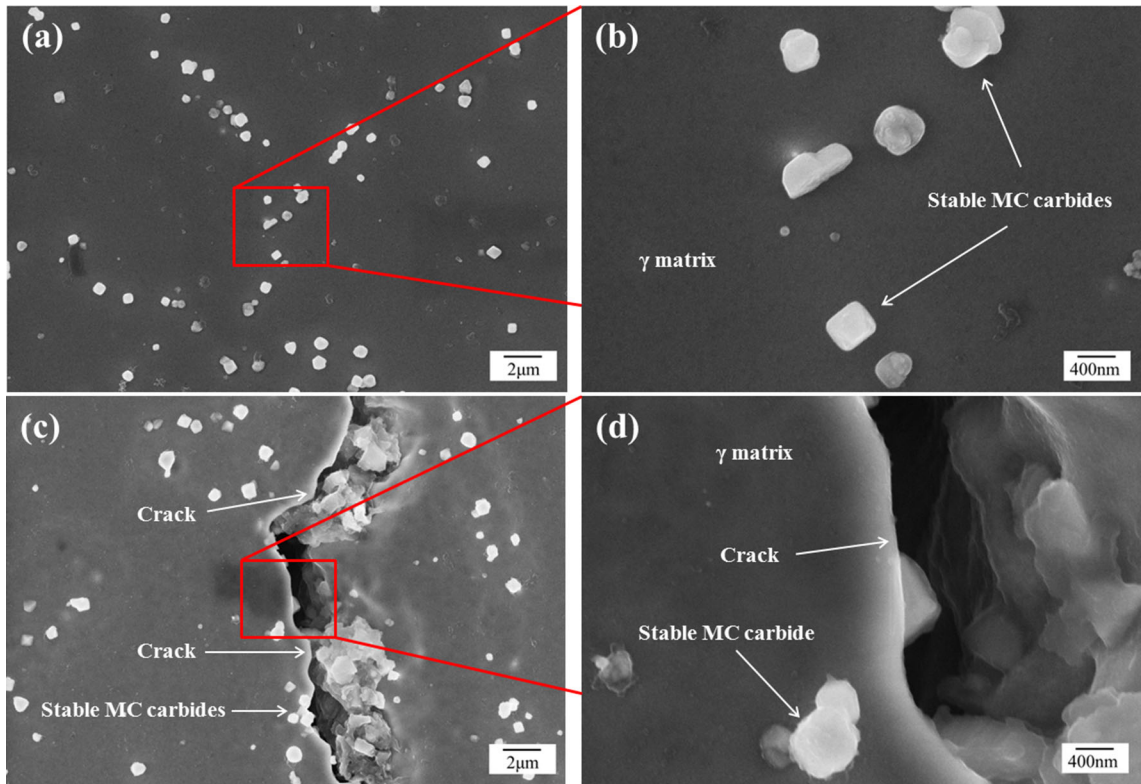
Fig. 6—Low- (*a* and *c*) and high- (*b* and *d*) magnification SEM micrographs showing the microstructure of the laser remelting in the HAZ close to the RZ.
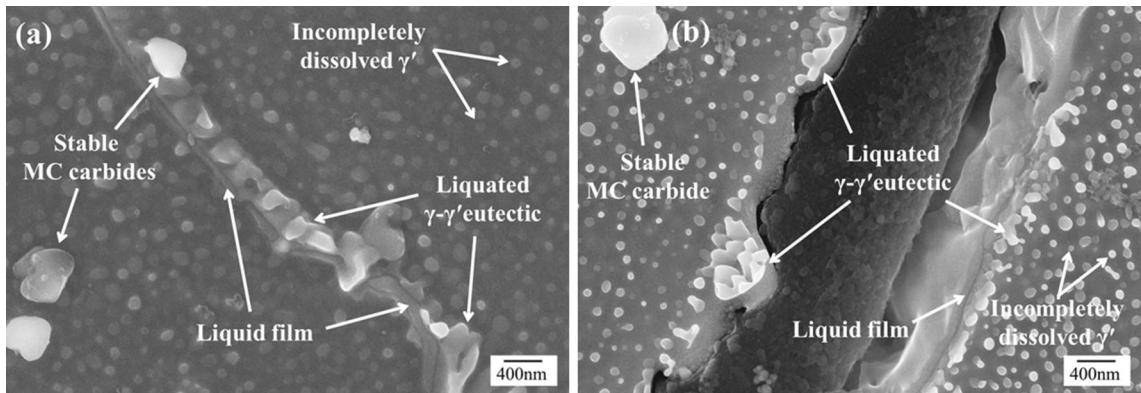

Fig. 7—SEM micrographs showing liquated γ-γ' eutectic (*a*) and cracked GB (*b*) in the HAZ located away from the RZ.

$$\frac{a_1}{3}\left(C_x^3 - C_{st}^{*3}\right) + \frac{a_2}{2}\left(C_x^2 - C_{st}^{*2}\right) + a_3\left(C_x - C_{st}^{*}\right)$$
$$= \left(\frac{(f_x - 1)(k - 1)}{k}\right)C_x - C_0 \qquad [10]$$

$$a_1 C_{st}^{*2} + a_2 C_{st}^{*} + a_3 = 0 \qquad [11]$$

$$a_1 C_x^2 + a_2 C_x + a_3 = f_x \qquad [12]$$

$$2a_1 C_{st}^{*} + a_2 = 1/\left(C_{st}^{*}(1 - k)\right) \qquad [13]$$

$$a_1 = \frac{2SC_x - SkC_x - SC_{st}^{*} - 1}{2kC_x^2 - 3C_x^2 - 2kC_{st}^{*}C_x + 4C_{st}^{*}C_x - C_{st}^{*2}}, \qquad [14]$$

where $S = 1/(kC_0(1 - k))$. Solving Eqs. [10]–[14], the five unknowns ($a_1, a_2, a_3, f_x,$ and c_x) above can be obtained and we can then estimate the solute segregation behavior and further formation process of the main phases of the IN-738LC alloy under the near-rapid solidification conditions. The equilibrium chemical composition of the MC, σ, and γ' phases in the IN-738LC alloy and the equilibrium partition coefficient (k_0) of the corresponding elements calculated by the Thermo-Calc software are listed in Table IV.
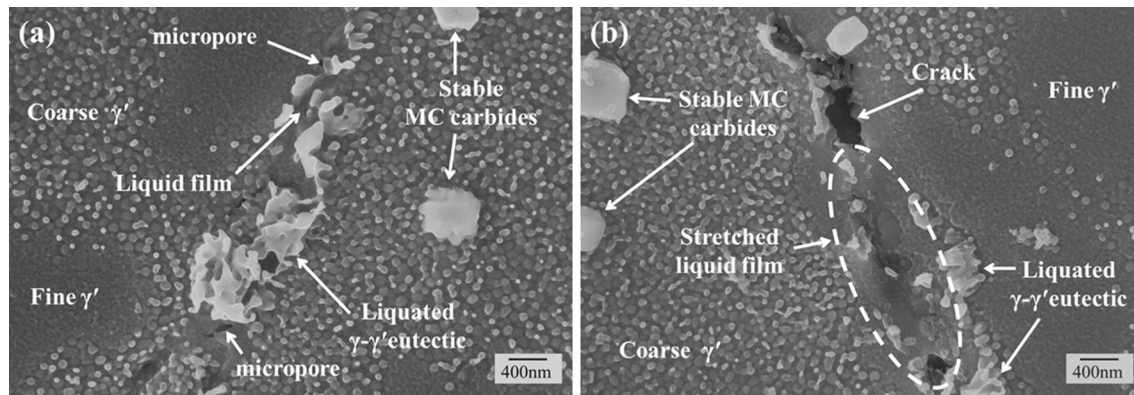
Fig. 8—Simulated HAZ microstructure showing the liquation of the γ-γ′ eutectic (*a*) and the stretched liquid film in the specimen heated to 1160 °C for 1 s (*b*).
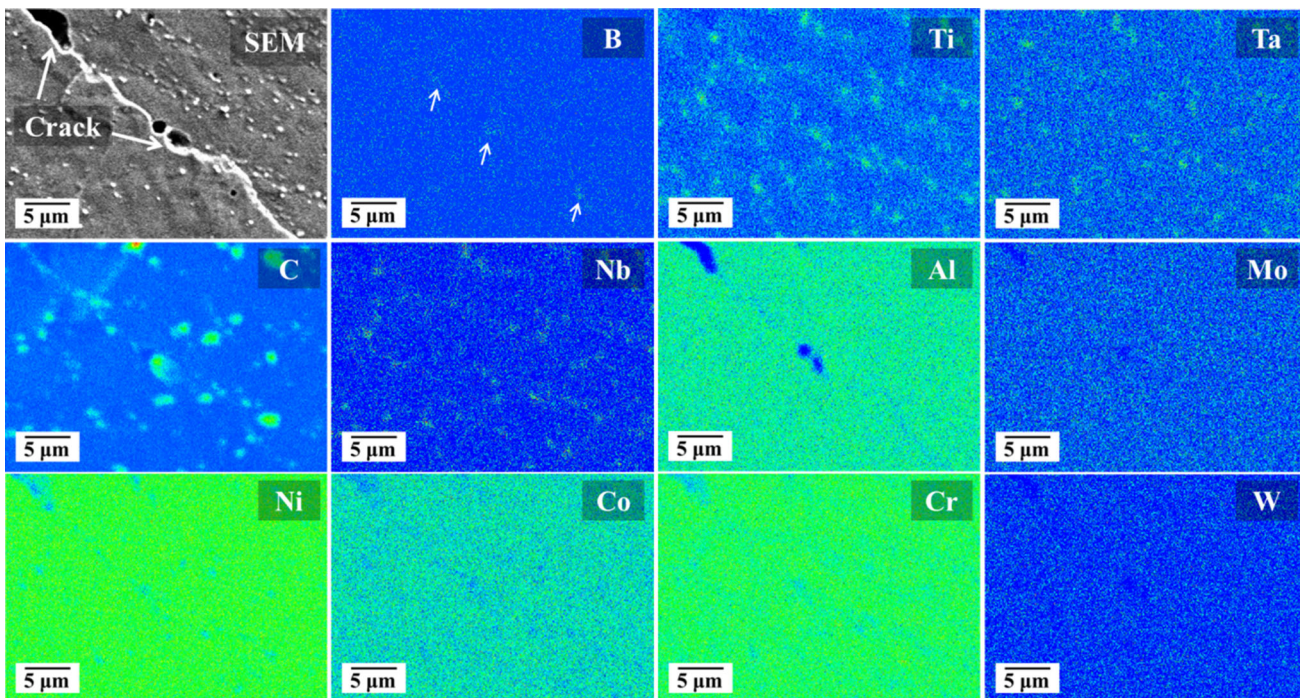

Fig. 9—The EPMA mapping results showing the elemental distribution around the GB near the crack in the LSF-fabricated IN-738LC specimen.

Table IV. Chemical Composition (Atomic Percent) of the Equilibrium MC, σ, and γ′ Phases and the Partition Coefficient (k_0) of Corresponding Elements as Calculated by Thermo-Calc Software Based on the Nominal Chemical Composition of the IN-738LC Alloy

Phase	Cr	Al	Ti	Mo	Co	Nb	Ta	C	Ni
MC	—	—	0.25	—	—	0.19	0.09	0.45	—
σ	0.60	—	—	0.11	0.11	—	—	—	0.17
γ′	0.04	0.08	0.13	—	0.04	0.03	0.01	—	0.64
k_0	0.986	1.012	0.672	0.720	1.115	0.325	0.414	0.120	—

Because the cracking is mainly related to liquation of the interdendritic precipitates (Figures 7 and 8), the segregation behavior of the main elements of the interdendritic precipitates is discussed in detail. Figures 10(a) shows the concentration profiles of elements enriched in the interdendritic region of the IN-738LC
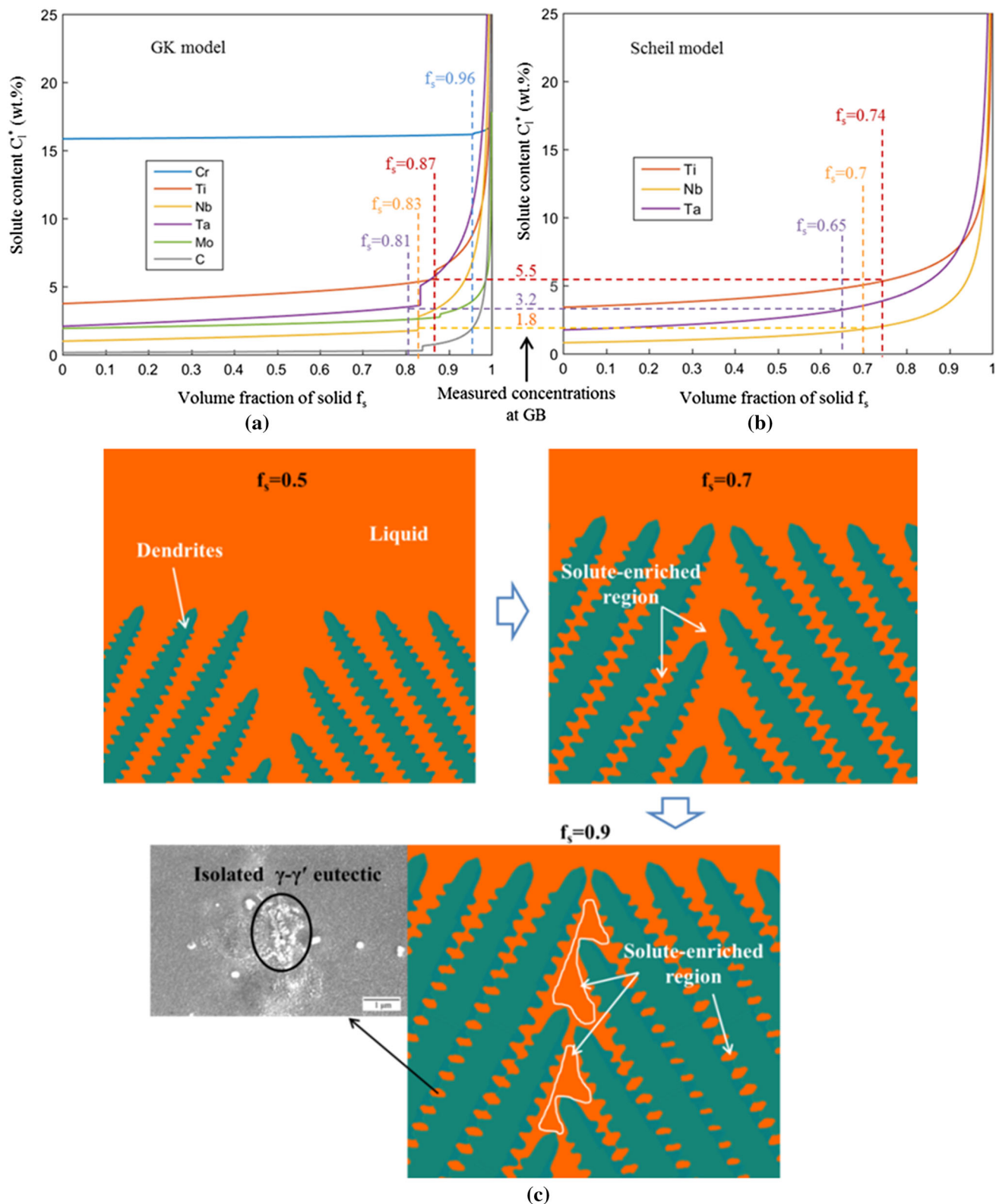
Fig. 10—Concentration profiles of elements enriched in the interdendritic region of the IN-738LC alloy as calculated by the GK model (*a*); concentration profiles of Ti, Nb, and Ta predicted by the Scheil model (*b*) are used for comparison; schematic illustration of the columnar dendritic solidification (*c*) and SEM image of the isolated γ-γ′ eutectic between the dendrites of the IN-738LC alloy (inset of (*c*)).

alloy as calculated by the GK model. Note that the carbide-forming elements (C, Ta, Nb, and Ti), which have smaller value of k_0 ($k_0 < 1$) than that of other elements according to Table IV, are first enriched in the liquid at the solid–liquid interface when f_s reaches ~ 0.8. This indicates that the composition of the interdendritic

liquid will first reach equilibrium between γ, MC, and the liquid. Thus, MC carbide and γ would form at the interdendrites over a range of temperatures via the $L \rightarrow \gamma + MC$ eutectic-type transformation, which is consistent with the results shown in Figure 3(b). However, the main σ phase-forming elements Cr, which has a k_0 value approximately equal to unity, begins to concentrate at the dendrites until $f_s \approx 0.96$ (Figure 10(a)). The formation of the σ phase could thus be suppressed owing to the rapid cooling during the LSF IN-738LC alloy. Ma et al.[39] have obtained a similar conclusion, whereby the rapid cooling will inhibit elemental segregation in their report regarding pulsed laser butt welding of Hastelloy C-276. In contrast, the γ-γ' eutectic would not be completely prevented by the rapid cooling process owing to the small k_0 values of Ti, Nb, and Ta which are also γ-γ' eutectic-forming elements,[40, 41] although Al has k_0 values of ~ 1.

In general, when the solidification rate is low, the solute segregation behavior can be approximately described by the Scheil model $\left(C_s^* = k_0 C_0 (1 - f_s)^{k_0 - 1} \right)$, based on the local equilibrium assumption.[38] Therefore, to better understand the formation of the γ-γ' eutectic at the end of the solidification process in LSF, the concentration profiles of Ti, Nb, and Ta were calculated by the Scheil model for comparison (Figure 10(b)). In addition, the average concentrations of Ti, Nb, and Ta (5.5, 1.8, and 3.2 wt pct, respectively) at the solute enrichment area (i.e., GB) obtained by EPMA are also shown in Figure 10(b). It is obvious that the solute enrichment initially appears in the residual liquid when f_s reaches 0.65, and as the solid fraction decreases further the degree of solute enrichment will increase more significantly according to the Scheil model (Figures 10(a) and (b)). The $L \rightarrow \gamma + \gamma'$ eutectic reaction will occur ($f_s \approx 0.74$) when the composition of the interdendritic liquid reaches equilibrium between the liquid, γ and γ', as shown in Figure 10(b). This process is illustrated in Figure 10(c), showing a schematic diagram of the dendritic growth and solute segregation at different stages of solidification. A coarse γ-γ' eutectic will finally form at the interdendritic region and the GB owing to the significant segregation and large dendritic spacing, similar to that in the cast IN-738LC alloy.[42] Nevertheless, the solute segregation behavior during LSF will be slightly different from that predicted by the Scheil model owing to the rapid cooling.[39] According to the GK model, the apparent enrichment of solutes in the liquid occurs only when f_s reaches between 0.81 and 0.87 (Figure 10(a)), which means that the composition conditions of the $L \rightarrow \gamma + \gamma'$ eutectic reaction may not be satisfied until the solidification is almost ended ($f_s \approx 0.87$). At this point, the secondary arms will almost be in contact with each other to form a small closed interdendritic region and the GB area will form a relatively semicontinuous liquid film owing to the most serious elemental segregation at the dendritic tip zone, as shown in Figure 10(c) ($f_s = 0.9$). Thus, an isolated γ-γ' eutectic is formed at the interdendritic region (inset of Figure 10(c)) and the semicontinuous γ-γ' eutectic is formed along the GB (Figures 4(a) and (b)) in the LSF-fabricated IN-738LC alloy. Sidhu et al.[34] have also presented a similar view in electron-beam-welding of the nickel-based superalloy IN-738LC.

B. Liquation Cracking Mechanism

1. Formation of continuous/semicontinuous liquid film along GB

The presence of a continuous/semicontinuous γ-γ' eutectic only at the GB provides the structural conditions for GB liquation cracking. Another important factor is the liquation of the γ-γ' eutectic in the LSF-fabricated IN-738LC alloy. For the large-sized γ' phase (usually 0.6 to 0.8 μm in castings[43]), it is difficult to completely dissolve the γ' phase during rapid heating. However, when the γ' phase is small (Figure 4) its dissolution rate will be significantly higher than that of the large-sized γ' phase.[12, 44] Once the γ' phase is completely dissolved before reaching the γ-γ' eutectic reaction temperature, the melting of the γ-γ' eutectic will not occur. Interestingly, the dissolution of the γ' phase in the HAZ changes in the direction away from the RZ (Figures 6 and 7). Figure 11(a) defines the different regions in the HAZ. The region near the RZ in the HAZ is called the completely dissolved zone (CDZ) and the region away from the RZ in the HAZ is called the incompletely dissolved zone (ICDZ), although the MC carbides in both zones seem to be unaffected during the laser remelting (Figures 6 and 7).

Accordingly, it is necessary to clarify the relationship between the dissolution of the γ' phase, the liquation of the γ-γ' eutectic, and the heating rate because of the existence of the zone in the HAZ wherein the γ' phase is completely dissolved (Figure 6). This can be discussed by means of Figure 11(b), which shows the temperature change trend in two regions of the HAZ, whereby $T_{\gamma'}$ is the starting solid dissolution temperature of γ' and $T_{\gamma-\gamma'}$ is the γ-γ' eutectic reaction temperature. It can be seen by comparing of Figures 7 and 4(b) that the γ-γ' eutectic in the ICDZ was liquated before the γ' phases were fully dissolved. This means that the γ' phases in the ICDZ could not be completely dissolved into the γ matrix in the time range $t_3 - t_4$ (although their sizes are as small as 50 to 100 nm), and neither do the γ' phases in CDZ in the time range $t_1 - t_2$ (i.e., < t$_3$-t$_4$). Therefore, the complete dissolution of the γ' phases in the CDZ (Figure 6) should be attributed to the fact that the CDZ experiences a higher temperature and longer heating time ($t_1 - t_6$) than the ICDZ ($t_3 - t_5$), as shown in Figure 11. The complete dissolution of the γ' phases in the CDZ would result in a supersaturated γ matrix, and the liquid phase formed by the liquation of the γ-γ' eutectic at this region would also be solidified epitaxially from a supersaturated γ matrix as the laser beam moves away. Thus, only the γ matrix and carbide can be observed and no obvious liquid film features can be found in this region (Figure 6). These results indicate that the γ-γ' eutectic in the HAZ of the LSF-fabricated IN-738LC will be easily remelted to form a liquid film once its temperature is above the eutectic reaction temperature during the laser remelting.
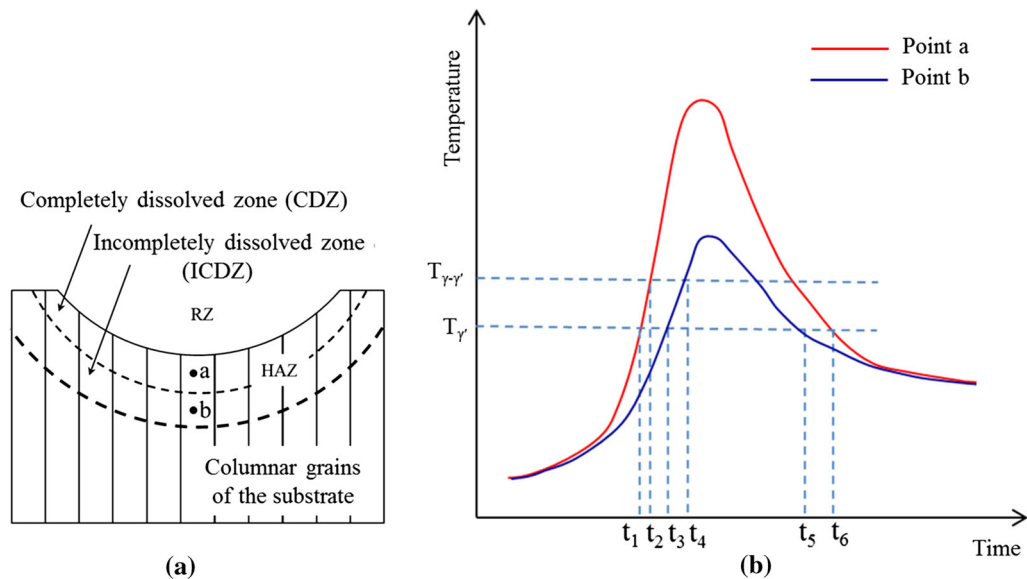
Fig. 11—Schematic diagram of laser remelting in the HAZ (*a*) and the temperature variation with time of the point "a" and "b" (*b*) marked in (a).

2. Effect of γ′ phase size on the formation mechanism of the liquid film (localized melting of γ-γ′ eutectic vs constitutional liquation of γ′ phase)

As mentioned above, the liquid film in the HAZ liquation cracking of γ′-strengthened superalloys generally forms in one of two ways: (i) localized melting of the γ-γ′ eutectic and (ii) constitutional liquation of the γ′ phase. However, it should be noted that there is no evidence indicating constitutional liquation of γ′ in the HAZ of the remelted IN-738LC alloy in this work, which is different from that observed in the welding of the cast IN-738LC alloy.[8]

However, as explicated earlier, the constitutional liquation of a secondary phase is closely related to its solid-state dissolution behavior. Radhakrishnan has found that the solid-state dissolution of coherent precipitates (*i.e.*, the γ′ phase in the IN-738LC alloy) is typically interface-controlled, in which the constitutional liquation may not occur.[14] This can be qualitatively illustrated by Figure 12, which shows how the interface-controlled dissolution affects the constitutional liquation during continuous heating. The dotted lines "a" and "b" in Figure 12 represent the solute concentration in the matrix at the γ′-γ interface corresponding to diffusion-controlled and interface-controlled liquation, respectively (Figure 12). According to Radhakrishnan,[14] in a superalloy with composition C_0 and with diffusion-controlled dissolution, the solute concentration in the γ matrix at the γ′−γ interface would deviate from equilibrium assuming it follows curve "a" during the continuous rapid heating. Thereupon, it would ultimately meet the solvus curve at temperature T_a, where the solute concentration in the γ matrix at the γ′−γ interface exceeds the bulk composition of the alloy. In this situation, the constitutional liquation (*i.e.*, a sub-solidus liquation) of the γ′ phase can occur. The typical characteristic of constitutional liquation of the γ′ phases during the welding of a cast IN-738LC alloy is the
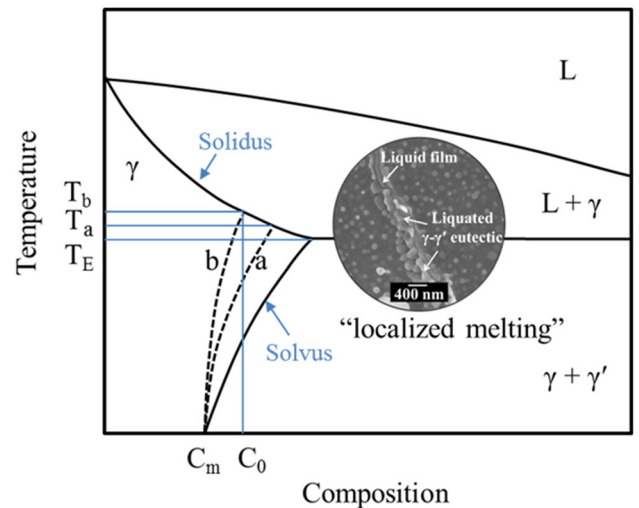

Fig. 12—Effect of interface-controlled dissolution on liquation temperature during continuous heating; inset shows the localized melting of the γ-γ′ eutectic in the LSF-fabricated IN-738LC alloy.

formation of fine re-solidified γ-γ′ eutectic product at the edge of the liquated γ′ particles.[45] However, for interface-controlled dissolution, the interface reaction should be more sluggish than that for diffusion-controlled dissolution, which would push the solvus curve further to the left of curve "a" (Figure 12). Therefore, curve "b" may intersect with the solidus curve at or even below the bulk composition of the alloy and, in this situation, matrix melting would occur and not constitutional liquation. In other words, no constitutional liquation would occur owing to the fact that the critical value of the solute concentration in the matrix for constitutional liquation cannot be reached.

Based on the discussion above, it can be deduced that the complete coherence (or lack thereof) of γ′ particle with the γ matrix is an important factor affecting the

constitutional liquation of the γ′ phase. Generally, there should exist a critical dimension of the γ′ and γ″ particles governing their coherence with the γ matrix in the precipitation-strengthened nickel-based superalloy, whereat once the particles exceed this critical dimension a loss of coherency occurs.[15–17] Czyrska-Filemonowicz[46] has found a similar phenomenon whereby a loss of coherency appears in nickel alloys after aging in the temperature range from 300 to 1000 °C. Iwamura[47] and Rastogi[48] also have found coherency loss of the Al₃Sc precipitates in the Al-0.2 wt pct Sc alloy and of the γ′ precipitates in the Ni-6.5 wt pct Si alloy during their coarsening. Therefore, it is reasonable to surmise that since the size of the γ′ particles at the GB in the cast IN-738LC alloy reaches 1 to 2 μm,[45] the γ′ phases may have lost its coherent relationship with the γ matrix. In addition, the dislocations typically cut the small-sized secondary phase particles while bowing out (i.e., so-called Orowan bowing) the large-sized ones and leaving dislocation loops around them. This indicates that dislocations will be more likely to pile up at the interface between the large-sized particles and the matrix, which could certainly also lead to coherency loss of the particles. Lachowicz[18] has reported a high dislocation density at the γ′-γ interfaces in the HAZ, that causes the γ′ lose their coherent relationship with the γ matrix and results in nucleation of microcracks during the welding of the cast Inconel 713C alloy. Thus, the dissolution of the γ′ phase in the cast IN-738LC alloy should be mainly diffusion-controlled, and thus the constitutional liquation of the γ′ phase is common in the welding of cast IN-738LC alloys.[8, 49, 50]

However, the size of the γ′ phase in the LSF-fabricated IN-738LC alloy, shown in Figure 4, is much smaller than that in cast specimens. Figures 13(a) and 13(b) show the dark-field TEM micrograph of γ′ precipitates in the LSF-fabricated IN-738LC and the diffraction pattern of the γ and γ′ phases from the [100] zone axis, respectively. The interplanar distances of the (002), (020) and (022) planes of the γ matrix are 1.771, 1.771, and 1.241 Å, respectively, which were then compared with the relative theoretical spacing for the γ matrix. The difference between the actual distances determined from the diffraction patterns and the theoretical values[18] for the γ matrix was 0.001 Å, while the difference of the angular values was 0°. The interplanar distance of the weak reflections in the [002] direction is 3.556 Å, which is characteristic for the (001) plane that belongs only to the γ′ phase and explicitly identifies this phase (Figure 13(a)). The lattice misfit coefficient, δ, for the γ and γ′ phases was calculated as 0.004 based on the following relationship:[51]

$$\delta = \frac{a_\text{p} - a}{a}, \qquad [15]$$

where a_p and a are the lattice parameters of the precipitates and the matrix phases, respectively. This calculated value of δ suggests that the γ′ phases have an excellent coherence with the γ matrix. Furthermore, the high-magnification images (Figures 13(c) through (e)) also clearly show the good coherent relationship between γ′ phase and γ matrix. Thus, it stands to reason

that the dissolution of the γ′ phases is interface-controlled, which would inhibit the occurrence of constitutional liquation according to the above discussion. Similarly, carbides that are incoherent with the matrix have been found to be constitutional liquated, while the fully coherent carbides were unaffected during the rapid heating of the alloy 800.[52] Though there is a theoretical possibility that fully coherent precipitates can avoid constitutional liquation, quantitative criteria for the constitutional liquation of coherent γ′ phases during the LSF of the IN-738LC alloy still require clarification in future work. Certainly, inhibition of constitutional liquation is actually helpful for the prevention of cracking. However, during the LSF of the IN-738LC, once the temperature exceeds the γ-γ′ eutectic reaction temperature (T_E), the small continuously distributed γ-γ′ eutectic along the GB would be directly melted, instead of constitutional liquation of the γ′ phase, to form the GB liquid film (inset of Figure 12). In addition, Sidhu et al.[34] have found that the high-angle GB typically has a relatively higher GB energy, which will cause the forming liquid film to further wet and penetrate the GB more easily, as well as to enhance the liquid film stability to a relatively lower temperature. Therefore, a continuous liquid film is more easily formed at the high-angle GB, which will be stretched to form cracks via tensile stress during cooling.

3. Effect of B enrichment at GB on the liquid film

Figure 9 demonstrates that B slightly enrichment exists at the GB, which indicates that borides may precipitate at the corresponding area. Figure 14(a) shows the TEM bright-field image revealing the irregular borides near the MC carbides. Analysis of the SADPs obtained from this boride (Figure 14(b)) indicates that it is a bct crystal structure of M_3B_2 with the lattice parameters $a = 0.571$ nm and $c = 0.305$ nm. As shown in Figure 14(c), these M_3B_2 borides precipitated along the GB. The appearance of the M_3B_2-type boride is consistent with the experimental observation by Ojo et al. in the welded IN-738LC alloy.[1,10,34,53] Further, a similar type of boride (M_3B_2) has been reported in the directionally solidified Ni-based superalloy IN-792.[54]

Generally, it is energetically more favorable for B atoms to segregate at loosely packed regions such as GBs, because this could help to reduce the free energy of such interfaces.[55] Boride is thus more likely to appear at the GBs, as shown in Figure 14. To further study the effect of B on the GB liquation, the solidification temperature range (STR) at different B contents was calculated using the Thermo-Calc software, which is shown in Figure 15. Owing to the inherent inability of EDS to analyze boron with sufficient accuracy, alloys with B contents ranging from 0 to 0.008 wt pct (nominal content in IN-738LC) were selected for further analysis based on the chemical composition of the IN-738LC alloy (Table I). It should be noted that even a very small increase in B content (0.003 wt pct) leads to a significant decrease in the equilibrium solidus temperature (Figure 15(a)), though with the further increase of B content the change of the solidus temperature becomes less obvious. Considering that the segregation of B
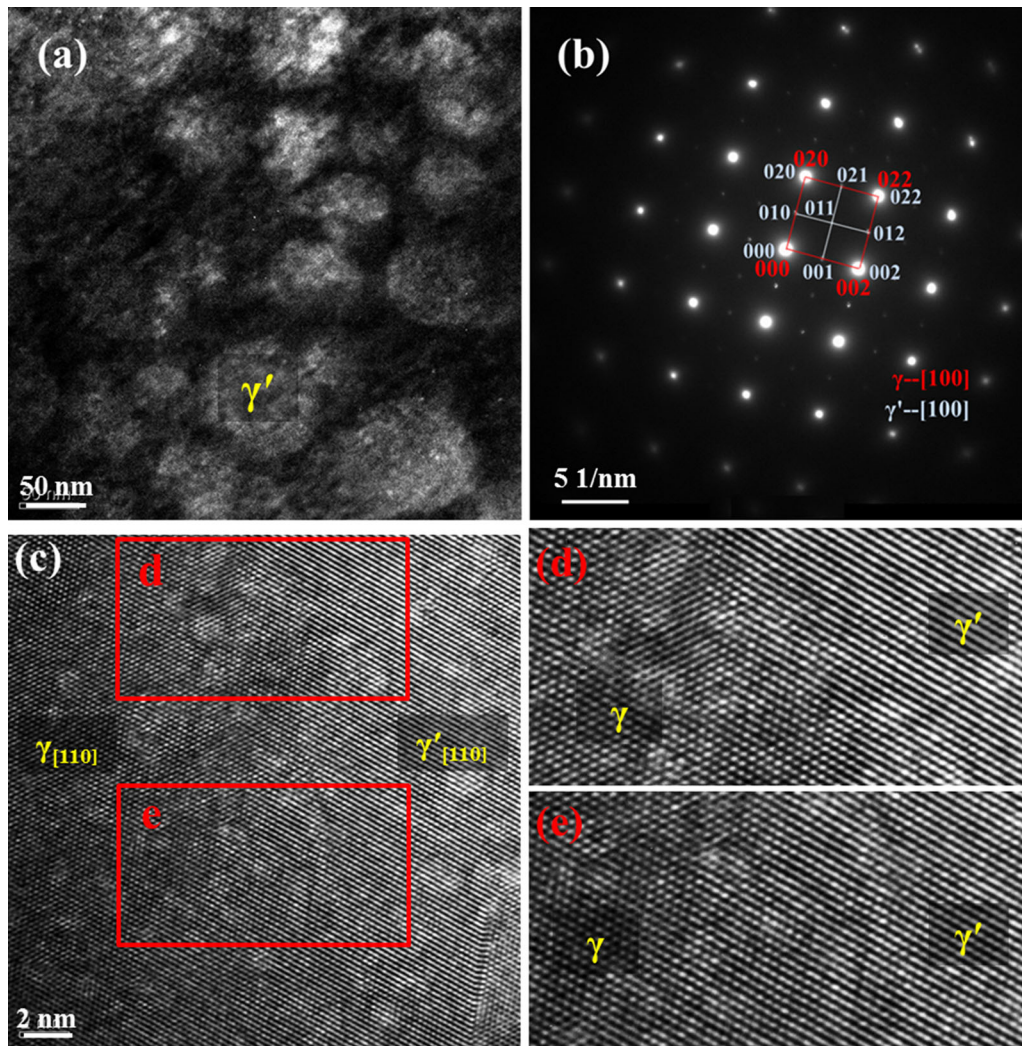
Fig. 13—Dark-field TEM image of the coherent γ′ precipitates and γ matrix (*a*) with SADP from [100] zone axis (*b*), high-resolution TEM image of the γ/γ′ interface (*c*), and the high-magnification images of the "d" (*d*) and "e" (*e*) regions marked in (*c*).

during cooling is of the non-equilibrium type in LSF, the solidification sequences were calculated by the Scheil model with different B contents (Figure 2(b)). It can be seen that the solidus temperature of IN-738LC is already very low owing to the presence of the low-melting γ-γ′ eutectic, and thus the effect of B content on the non-equilibrium STR is not significant. Even so, a small content of B (0.001 wt pct) could still reduce the non-equilibrium solidus temperature by 6 °C. These results can be attributed to the fact that B is known as a depressing element for the alloy melting point, which could lower the solidification temperature in nickel-based superalloys.[56] In other words, whether it is under equilibrium or non-equilibrium conditions, the B enrichment will cause the corresponding regions to be melted more easily during the continuous heating. Accordingly, during the subsequent deposition, the enrichment of B at the GB in the already-deposited layer would further reduce the initial GB liquation temperature, which would make the liquid film easier to form at the GB than within the grains. Egbewand and Osoba have also

found that the rapid decomposition of the boride particles during the welding heating cycle will lead to the liberation of boron atoms, which could significantly reduce the starting temperature of GB liquation.[43,57]

In fact, even for very small amounts of B, the B enrichment in the superalloy can promote the liquation of adjacent areas and the formation of liquid film, while it can also affect the stability of the liquid film.[58] It is known that B has the ability to reduce the solid/liquid interface energy, which can promote cracking by extensive wetting of the solid dendrites when the liquid film is still present during the very last stage of solidification.[58,59] Zhang *et al.* have also held a similar viewpoint that the enrichment of B may lower the surface tension of the residual liquid phase, which would cause the liquid film to continuously wet the GB to very low temperatures during the cooling.[60,61] The reduction of the terminal solidification temperature during cooling could in effect enlarge the brittle temperature range, within which the HAZ exhibits a negligible ductility during the weld cooling;[62] and could delay the ductility
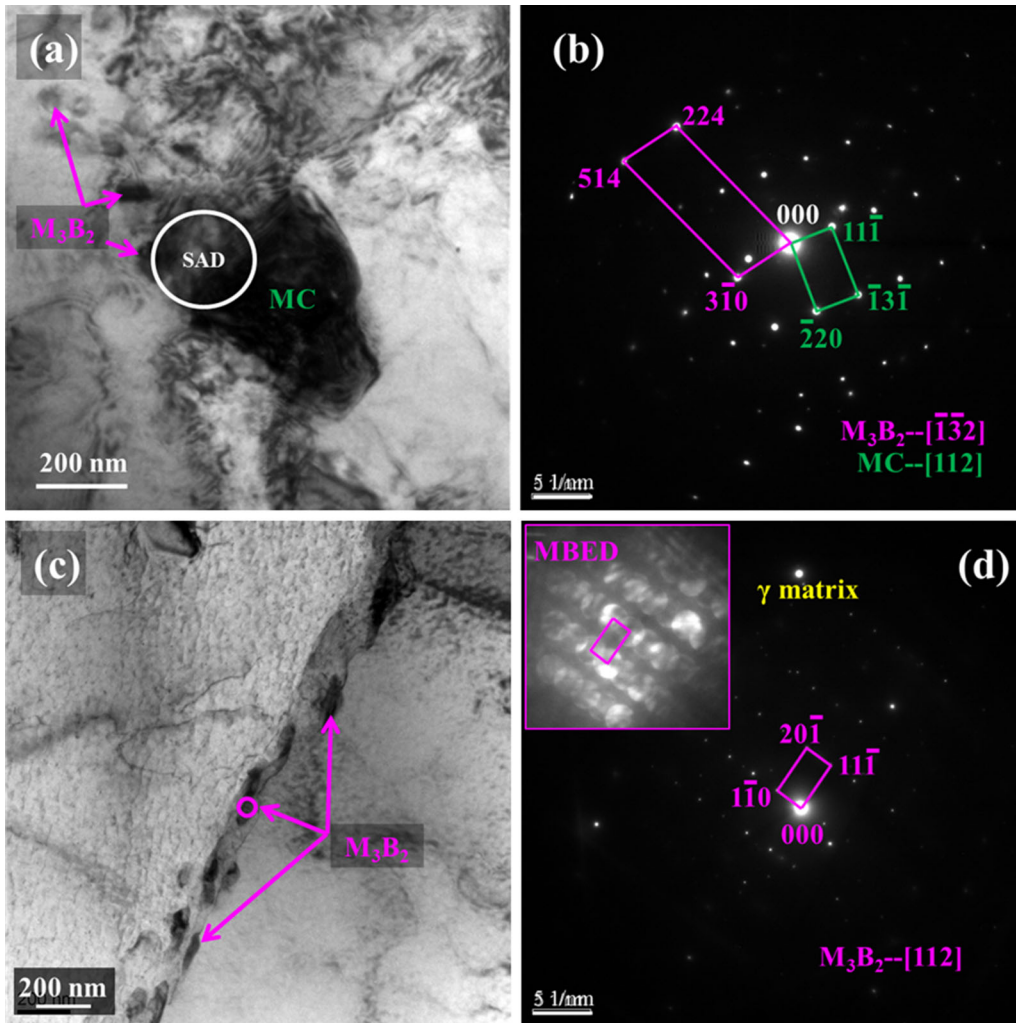
Fig. 14—TEM micrograph showing the M_3B_2 near the MC carbide (*a*); SADP from the M_3B_2 taken along the $[\bar{1}32]$ zone axis and from the MC taken along the [112] zone axis (*b*) and TEM micrograph showing the M_3B_2 (*c*) with SADP taken along the [112] zone axis (*d*) along the GB. Inset is the microbeam electron diffraction taken from the circle marked in (c).
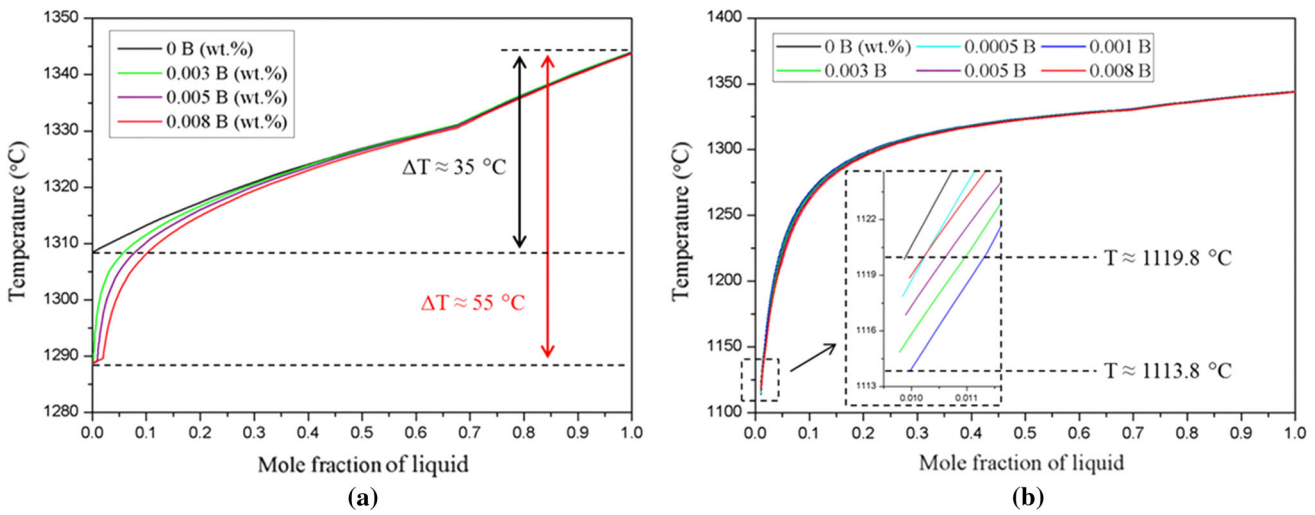

Fig. 15—Equilibrium phase diagram as predicted by Thermo-Calc (*a*) and solidification sequences as calculated by the Scheil model (*b*) with different B contents based on the chemical composition of the IN-738LC alloy.

recovery in the HAZ, which may promote susceptibility to liquation cracking.

4. Stress in HAZ required to trigger liquation cracking

The discussion above mainly considers the liquation cracking in terms of the formation of a liquid film and its influencing factors. However, another critical factor leading to the HAZ cracking still requires clarification, i.e., stress in the HAZ of the deposit. It is well known that the main mechanical driving force for hot cracking is the tensile stress (mainly thermal stress) generated during the LSF. In general, thermal stress mainly results from the accommodation of thermal expansion and subsequent contraction, which is caused by severe thermal excursions and steep thermal gradients local to the deposited material during LSF. After the deposition, the thermal stress that is not eventually released in the deposits will ultimately form the residual stress.[63, 64] Since the thermal stress is so closely related to the residual stress, it is reasonable to estimate the thermal stress during LSF by estimating the residual stress in the LSF-fabricated IN-738LC deposits. It is worth mentioning that, although microstructural differences exist in the dendrite core/interdendritic region and the overlapping zone/inner-track zone, the residual stress measured by the Vickers micro-indentation method can truly reflect the stress state of the LSF-fabricated specimens, as reported in References 11, 25, 26 and 65. It is necessary to point out that the width of the HAZ, in which there exists an obvious non-uniform distribution of γ' phases, in the remelted deposit was ~ 200 μm (Figure 5(a)), while the diagonal length of the indentation herein can be ~ 50 μm. Thus, the indentation will hit a small bulk zone wherein the amount of γ' will not be significantly lower or higher than the nominal amount, since the amount of γ' should gradually change from the RZ to the substrate zone. In addition, the microhardness changes slightly in the HAZ (Figure 16(c)), which indicates that the strength of the corresponding area may exhibit a similar trend owing to the fact that the microhardness is approximately proportional to the tensile strength.[66] Thus it is reasonable to assume that the K and n values in the HAZ can be obtained using a bulk stress–strain curve with the power-law function ($\sigma = K\varepsilon_p^n$), which are 1425.6 and 0.1001, respectively. The tensile stress–strain curve of the LSF-fabricated IN-738LC alloy and the fitted curve are shown in Figure 16(a). Substituting K and n into Eqs. [3] and [4], they were then transformed into Eqs. [16] and [17], respectively.

$$\varepsilon_{res} = \left(\frac{H}{3 \times 1425.6}\right)^{1/0.1001} - 0.08 \qquad [16]$$

$$\varepsilon_{res} = 1425.6 \times |\varepsilon_{res}|^{0.1001} \times \left[\exp\left(\frac{c^2 - 1}{0.32}\right) - 1\right] \qquad [17]$$

To ensure that the indentations do not affect each other in the narrow HAZ (shown in Figure 5(a)), the microhardness was obtained every 100 μm from the

substrate to the RZ, as shown in Figures 16(b) and (c). It can be seen that the microhardness in the HAZ and RZ is a little lower than in the substrate. Comparing Figures 6 and 7 it is obvious that the γ' phases in the HAZ experience both complete and incomplete solid dissolution, which reduces their size and leads to the decrease of the microhardness in the HAZ. In addition, the γ' phases in the RZ do not have enough time to precipitate and increase in size without subsequent reheating cycles after the remelting, which typically causes them to exhibit small sizes or even prevents them from precipitating.[5] The microhardness is thus relatively low in the RZ, as shown in Figure 16(c).

The residual stress can be obtained by substituting the microhardness into Eqs. [16] and [17], whose variation from the substrate to the RZ is also presented in Figure 16(c). It should be noted that the obtained residual stress values may be lower than the actual values owing to the following factors: first and foremost, part of the residual stress will be relaxed during cutting and polishing of the specimen. Next, part of the residual stress in the specimen will be relaxed as the indenter presses into the specimen. In addition, part of the residual stress in the LSF-fabricated specimen could be relaxed owing to the multiple cycles of laser scanning and heating, which are equivalent to an annealing treatment. Finally, some assumptions made herein and the microhardness and indentation area measurements will inevitably lead to some error. However, similar to the reported works on Ni-based superalloys,[11,25] an overall lowering of the data should not affect the main purpose here of measuring residual stress. This is because, with the qualitative comparison of the level of residual stress in the RZ, HAZ, and substrate zone of the remelted deposit, the residual stress of each position in the section should be similarly affected and its distribution in the section should be similar to the original. It can be found that the distribution of the residual stress is non-uniform, and especially in the HAZ. In general, the high cyclic heating and cooling regime caused by the moving heat source makes the LSF process vulnerable to thermal stresses.[25,67] The substrate (i.e., LSFed IN-738LC specimen) will certainly possess a certain residual stress. The RZ also exhibits a high residual stress owing to the high thermal stresses and solidification shrinking stress generated during the rapid solidification of the molten pool.[68,69] The high residual stress existing in the HAZ could be attributed to two factors. First, owing to the close proximity of the HAZ and the RZ, the temperature in the HAZ changes drastically and induces high thermal stress. Second, the non-uniform phase transformation process (non-uniform solution and precipitation of γ' phases shown in Figures 6 and 7) in the HAZ during the rapid thermal cycling produces a phase transformation stress.[70] It is generally known that the strains existing in regions with different microstructures are generally different under identical stress levels,[71] and the stress concentration is thus more likely to occur in areas with non-uniform microstructures (i.e., the HAZ). Paddea has also found that the highest tensile stress exists in the HAZ during the welding of P91 steel.[72] Because the true driving
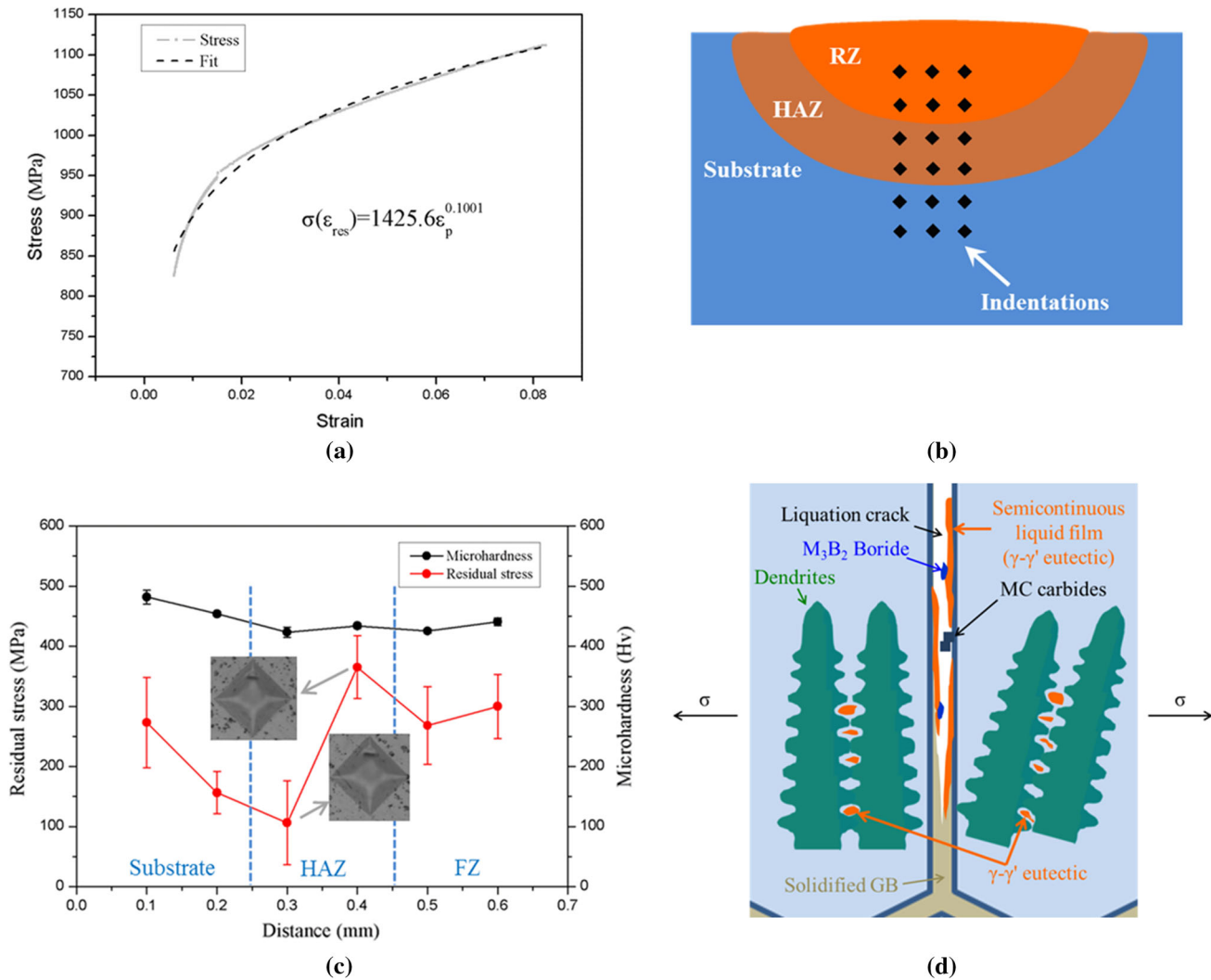
Fig. 16—Tensile stress–strain curve of the LSF-fabricated IN-738LC alloy and its power-law fit (*a*); schematic diagram of the microhardness measurement position (*b*) and the corresponding results of microhardness and residual stress (*c*); schematic diagram of the GB liquation cracking mechanism of the HAZ (*d*).

force of cracking is the real-time thermal stress during LSF, finite element simulations and real-time measurements of the thermal stress are needed in future works to obtain a deeper understanding of the cracking driving force.

Figure 16(d) shows the GB liquation cracking mechanism in the HAZ of the LSF-fabricated IN-738LC alloy. It can be seen that the liquid films formed by the liquation of the isolated γ-γ' eutectic areas are prevented from connecting to each other owing to the obstruction of the dendritic arms. The liquid film formed at the GB exhibits a relatively continuous distribution, however, which can be attributed to three factors. The first factor is the semicontinuous distribution exhibited by the γ-γ' eutectic (shown in Figure 4). The second factor is the presence of borides at the GB. Finally, the last factor is the greater wettability of the GB compared to that of the interdendritic region inside the grain, which causes the liquid film to spread easier along the GB.[34] Once the liquid film is formed, it will stretch under the tensile

stress induced by the non-uniform phase transformation and the rapid heating and cooling,[73,74] and thus form micropores (shown in Figure 8(a)). These micropores will continue to expand under the tensile stress until ultimately resulting in cracking (Figures 8(b) and 10(c)).

V. CONCLUSIONS

The laser remelting of the IN-738LC alloy deposit prepared by LSF was carried out and the HAZ liquation cracking mechanism was studied in detail considering element segregation, enrichment of trace elements, γ' phase size, and residual stress. The main conclusions are as follows:

1. The apparent enrichment of the γ-γ' eutectic-forming elements in the liquid occurs only when the solid fraction (f_s) reaches ~ 0.87 during the solidification in the LSF of IN-738LC, according to the

calculated results by the GK and Scheil models and the EPMA results. This elemental enrichment at the last stage of solidification leads to the formation of a large amount semicontinuous γ-γ' eutectic along the GB and of isolated γ-γ' eutectic within the grains in the LSF-fabricated IN-738LC alloy.

2. The cracks are consistently found to propagate along the GB of the LSF-fabricated IN-738LC alloy, which can be attributed to two factors: (1) Localized melting of the semicontinuous γ-γ' eutectic during subsequent depositions would induce the formation of a continuous liquid film along the GB of the LSF-fabricated IN-738LC. (2) Boron is found to slightly segregate at the GB of the LSF-fabricated IN-738LC, and even a very small increase in B content results in a significant decrease in the GB liquation temperature of IN-738LC.

3. The ~ 100 nm-diameter γ' precipitates in the LSF-fabricated IN-738LC alloy are found to be completely coherent with the γ matrix, which could inhibit the occurrence of constitutional liquation of the γ' phases in the LSF-fabricated IN-738LC according to the prediction by a simplified binary phase diagram.

4. The microhardness in the HAZ (~ 428 HV) of the LSFed IN-738LC alloy is a little lower than that in the substrate (~ 465 HV) and RZ (~ 433 HV), which is found to be primarily governed by the amount and the size of the γ' phases. The residual stress in the HAZ, as estimated by the Vickers micro-indentation method, is high and non-uniform (100 to 360 MPa). This could indicate that the thermal stress, which is the main driving force for HAZ liquation cracking in the LSF-fabricated IN-738LC alloy, is also high and non-uniform.

REFERENCES

1. O.A. Ojo, N.L. Richards, and M.C. Chaturvedi: *Metall. Mater. Trans. A*, 2006, vol. 37, pp. 421–33.
2. M.F. Chiang and C. Chen: *Mater. Chem. Phys.*, 2009, vol. 114, pp. 415–19.
3. X. Lin, H.O. Yang, J. Chen, and W.D. Huang: *Acta Metall. Sin.*, 2006, vol. 42, pp. 361–68.
4. P. Guo, X. Lin, J. Li, Y. Zhang, M. Song, and W. Huang: *Corros. Sci.*, 2017, vol. 132, pp. 79–89.
5. J. Chen and L. Xue: *Mater. Sci. Eng., A*, 2010, vol. 527, pp. 7318–28.
6. L. Rickenbacher, T. Etter, S. Hövel, and K. Wegener: *Rapid Prototyp. J.*, 2013, vol. 19, pp. 282–90.
7. X. Zhao, X. Lin, J. Chen, L. Xue, and W. Huang: *Mater. Sci. Eng., A*, 2009, vol. 504, pp. 129–34.
8. O.A. Ojo and M.C. Chaturvedi: *Mater. Sci. Eng., A*, 2005, vol. 403, pp. 77–86.
9. O.A. Ojo, Y.L. Wang, and M.C. Chaturvedi: *Mater. Sci. Eng., A*, 2008, vol. 476, pp. 217–23.
10. M. Montazeri and F.M. Ghaini: *Mater. Charact.*, 2012, vol. 67, pp. 65–73.
11. Y.L. Hu, X. Lin, K. Song, X.Y. Jiang, H.O. Yang, and W.D. Huang: *Optics & Laser Technol.*, 2016, vol. 86, pp. 1–7.
12. O.T. Ola, O.A. Ojo, and M.C. Chaturvedi: *Philos. Mag.*, 2014, vol. 94, pp. 3295–16.
13. J.J. Pepe and W.F. Savage: *Welding J. Res. Suppl.*, 1967, vol. 46, p. 411.
14. B. Radhakrishnan: *Interface Sci.*, 1993, vol. 1, pp. 175–82.
15. A. Devaux, L. Naze, R. Molins, A. Pineau, A. Organista, J.Y. Guedou, J.F. Uginet, and P. Heritier: *Mater. Sci. Eng., A*, 2008, vol. 486, pp. 117–22.
16. Y. Ji, Y. Lou, M. Qu, J.D. Rowatt, F. Zhang, T.W. Simpson, and L.Q. Chen: *Metall. Mater. Trans. A*, 2016, vol. 47, pp. 3235–47.
17. G.C. Weatherly and R.B. Nicholson: *Philos. Mag.*, 1968, vol. 17, pp. 801–31.
18. M. Lachowicz, W. Dudziński, and M. Podrez-Radziszewska: *Mater. Charact.*, 2008, vol. 59, pp. 560–66.
19. G. Bi, C. Sun, H. Chen, F.L. Ng, and C.C.K. Ma: *Mater & Des.*, 2014, vol. 60, pp. 401–08.
20. X. Zhao, J. Chen, F. He, H. Tan, and W. Huang: *Rare Metal. Mat. Eng.*, 2007, vol. 36, pp. 216–20.
21. J. Yang, F. Li, Z. Wang, and X. Zeng: *J. Mater. Process. Tech.*, 2015, vol. 225, pp. 229–39.
22. J. Xu, X. Lin, P. Guo, Y. Hu, X. Wen, L. Xue, J. Liu, and W. Huang: *Mater. Sci. Eng., A*, 2017, vol. 691, pp. 71–80.
23. S. Suresh and A.E. Giannakopoulos: *Acta Mater.*, 1998, vol. 46, pp. 5755–67.
24. C. Chen, C.X. Pan, and F.U. Qiang: *Mater. Mech. Eng.*, 2007, vol. 31, pp. 8–11.
25. F. Liu, X. Lin, G. Yang, M. Song, J. Chen, and W. Huang: *Opt. Laser Technol.*, 2011, vol. 43, pp. 208–13.
26. X. Wang, D. Deng, H. Yi, H. Xu, S. Yang, and H. Zhang: *Opt. Laser Technol.*, 2017, vol. 92, pp. 5–14.
27. S. Carlsson and P.L. Larsson: *Acta Mater.*, 2001, vol. 49, pp. 2179–91.
28. A. Chamanfar, M. Jahazi, A. Bonakdar, E. Morin, and A. Firoozrai: *Mater. Sci. Eng., A*, 2015, vol. 642, pp. 230–40.
29. A. Bonakdar, M. Molavi-Zarandi, A. Chamanfar, M. Jahazi, A. Firoozrai, and E. Morin: *J. Manuf. Process.*, 2017, vol. 26, pp. 339–54.
30. N. Saunders, M. Fahrmann, and C.J. Small: in *Superalloys 2000*, K.A. Green, T.M. Pollock, and R.D. Kissinger, eds., TMS, Warrendale, 2000, pp. 803–11.
31. Y. Liang, X. Cheng, and H. Wang: *Acta Mater.*, 2016, vol. 118, pp. 17–27.
32. Y. Danis, C. Arvieu, E. Lacoste, T. Larrouy, and J. Quenisset: *Mater. Des.*, 2010, vol. 31, pp. 402–16.
33. A. Basak and S. Das: *J. Alloy. Compd.*, 2017, vol. 705, pp. 806–16.
34. R.K. Sidhu, O.A. Ojo, and M.C. Chaturvedi: *Metall. Mater. Trans. A*, 2007, vol. 38, pp. 858–70.
35. S.M. Seo, J.H. Lee, Y.S. Yoo, C.Y. Jo, H. Miyahara, and K. Ogi: *Metall. Mater. Trans. A*, 2011, vol. 42, pp. 3150–59.
36. B Giovanola and W Kurz: *Metall. Trans. A*, 1990, vol. 21, pp. 260–63.
37. W Kurz, B Giovanola, and R Trivedi: *Acta Metall.*, 1986, vol. 34, pp. 823–30.
38. W Kurz and DJ Fisher: *Fundamentals of Solidification*, Trans Tech Publications, Zürich, 1992, pp. 106–07.
39. G Ma, D Wu, and D Guo: *Metall. Mater. Trans. A*, 2011, vol. 42A, pp. 3853–57.
40. GH Gessinger and MJ Bomford: *Powder Metallurgy of Superalloys, Butterworths Monographs in Materials*, Butterworth and Co., London, 1984, pp. 51–76.

41. J Guo: *Materials Science and Engineering for Superalloys*, Science Press, Beijing, China, 2008, pp. 89–102.
42. N El-Bagoury, M Waly, and A Nofal: *Mater. Sci. Eng: A*, 2008, vol. 487, pp. 152–61.
43. AT Egbewande, HR Zhang, RK Sidhu, and OA Ojo: *Metall. Mater. Trans. A*, 2009, vol. 40, pp. 2694–2704.
44. HB Aaron and GR Kotler: *Metall. Trans.*, 1971, vol. 2, pp. 393–408.
45. OA Ojo, NL Richards, and MC Chaturvedi: *Scr. Mater.*, 2004, vol. 50, pp. 641–46.
46. A Czyrska-Filemonowicz: *Polish Acad. Sci.*, 1989, vol. 32, pp. 32–57.
47. S Iwamura and Y Miura: *Acta Mater.*, 2004, vol. 52, pp. 591–600.
48. PK Rastogi and AJ Ardell: *Acta Metall.*, 1971, vol. 19, pp. 321–30.
49. OT Ola, OA Ojo, and MC Chaturvedi: *Mater. Sci. Technol.*, 2013, vol. 29, pp. 426–38.
50. OT Ola, OA Ojo, and MC Chaturvedi: *Mater. Sci. Tech.-Lond.*, 2013, vol. 30, pp. 1461–69.
51. AJ Ardell: *Pergamon Press*, 1963, vol. 16A, pp. 2131–65.
52. AD Romig, JC Lippold, and MJ Cieslak: *Metall. Trans. A*, 1988, vol. 19, pp. 35–50.
53. OA Ojo, NL Richards, and MC Chaturvedi: *Scr. Mater.*, 2004, vol. 51, pp. 683–88.
54. SM Seo, IS Kim, JH Lee, CY Jo, H Miyahara, and K Ogi: *Metall. Mater. Trans. A*, 2007, vol. 38, pp. 883–93.
55. X Huang, MC Chaturvedi, NL Richards, and J Jackman: *Acta Mater.*, 1997, vol. 45, pp. 3095–3107.
56. RT Holt and W Wallace: *Metall. Rev.*, 1976, vol. 21, pp. 1–24.
57. LO Osoba, RK Sidhu, and OA Ojo: *Mater. Sci. Technol.*, 2013, vol. 27, pp. 897–902.
58. E Chauvet, P Kontis, EA Jägle, B Gault, D Raabe, C Tassin, J Blandin, R Dendievel, B Vayre, S Abed, and G Martin: *Acta Mater.*, 2018, vol. 142, pp. 82–94.
59. J. N. Dupont, J. C. Lippold, S. D. Kiser: Welding Metallurgy and Weldability of Nickel-Base Alloys, in: Wiley (Ed.), 2011, pp. 225–43.
60. BJ Keene: *Metall. Rev.*, 1993, vol. 38, pp. 157–92.
61. J Zhang and RF Singer: *Metall. Mater. Trans. A*, 2004, vol. 35, pp. 1337–42.
62. W Lin, JC Lippold, and WAI Baeslack: *Weld. J.*, 1993, vol. 72, pp. 135–53.
63. RJ Moat, AJ Pinkerton, L Li, PJ Withers, and M Preuss: *Mater. Sci. Eng: A*, 2011, vol. 528, pp. 2288–98.
64. YC Tsui and TW Clyne: *Thin Solid Films*, 1997, vol. 306, pp. 23–33.
65. J Cao, F Liu, X Lin, C Huang, J Chen, and W Huang: *Optics Laser Technol.*, 2013, vol. 45, pp. 228–35.
66. P Zhang, SX Li, and ZF Zhang: *Mater. Sci. Eng: A*, 2011, vol. 529, pp. 62–73.
67. M Alimardani, E Toyserkani, JP Huissoon, and CP Paul: *Opt. Laser. Eng.*, 2009, vol. 47, pp. 1160–68.
68. Z Feng, T Zacharia, and SA David: *Weld. J.*, 1997, vol. 76, pp. S470–83.
69. SS Babu, SA David, JW Park, and JM Vitek: *Sci. Technol. Weld. Join.*, 2004, vol. 9, pp. 1–12.
70. K Zhao, YH Ma, LH Lou, and ZQ Hu: *J. Mater. Res.*, 2005, vol. 20, pp. 2314–21.
71. AT Egbewande, RA Buckson, and OA Ojo: *Mater. Charact.*, 2010, vol. 61, pp. 569–74.
72. S Paddea, JA Francis, AM Paradowska, PJ Bouchard, and IA Shibli: *Mater. Sci. Eng: A*, 2012, vol. 534, pp. 663–72.
73. JX Fang, SY Dong, YJ Wang, BS Xu, ZH Zhang, D Xia, and P He: *Mater. Des.*, 2015, vol. 87, pp. 807–14.
74. NJ Harrison, I Todd, and K Mumtaz: *Acta Mater.*, 2015, vol. 94, pp. 59–68.